Department of Precision and Microsystems Engineering

Dynamic performance evaluation of two-axis lathes

A.D. Schoneveld

Report no : 2023.051
Supervisor : Dr. G.J. Verbiest
Specialisation : Mechatronic System Design
Type of report : MSc Thesis
Date : August 2023

Dynamic performance evaluation of two-axis lathes

by

A.D. Schoneveld

to obtain the degree of Master of Science
at the Delft University of Technology,
to be defended publicly on Monday August 21, 2023 at 13:00.

Student number:	4395980	
Project duration:	October 4, 2021 – August 21, 2023	
Thesis committee:	Dr. G. J. Verbiest,	TU Delft, supervisor
	Dr. ir. R. A. J. van Ostayen,	TU Delft
	Ir. B. de Wolf,	Hembrug Danobat

An electronic version of this thesis is available at `http://repository.tudelft.nl/`.

TU Delft

Preface

Soon after I started my bachelor in 2014, I was introduced to the manual mills and lathes that were part of the university machine shop. Not long after, I took every opportunity to operate these magnificent machines - turning metal into chips, scrap and sometimes even functional workpieces. As the years went by, the designs became more elaborate and more focused on function and manufacturability. Spending a year designing and building a Formula Student racecar kicked this obsession into overdrive, as I soon spent many days (and nights) operating the abused-but-beautiful Maho MH500W CNC mill.

The affection for subtractive manufacturing expanded into designing mechanisms and machines, soon developing great interest in precision mechanics and ultimately culminating into being admitted to the High Tech Engineering track of the Mechanical Engineering masters program. I am happy to say that all three of these major interests have come together in this thesis.

First and foremost, I would like to thank my university and company supervisors; Dr. Gerard Verbiest and Ir. Bart de Wolf. Your guidance and patience was paramount throughout the past two years. I would also like to thank all Hembrug, Danobat and Ideko staff for their support. My thanks also goes out to Ir. Milan Vermeulen, for spending several evenings together going over our theses.

Additionally, I would like to thank Josh Hacko and Adam Demuth for unknowingly introducing me to Hembrug through their podcast *The Precision Microcast*, a podcast I'd happily recommend to anyone interested in precision mechanics. I would also like to thank the gears, whose support works in mysterious ways, and Osmium, for always being in the top-right corner.

Finally, I would like to dedicate this thesis to my son, without whom this thesis would have been finished months earlier, and to my partner, without whom this thesis would have been finished months later.

A.D. Schoneveld
Leiden, August 2023

Contents

Abstract

With the increasing demand for extended service life and increased precision and accuracy of precision mechanics across various industries, machine tool manufacturers face the challenge of increasing the performance of their machines. To achieve this goal, the performance of the machines must be evaluated, points of improvement must be identified and subsequently be acted on.

This thesis is focused on the evaluation of the dynamic performance of a two-axis CNC lathe, subject to vibration modes excited by movement of the machine axes. To this end, two experiment setups are designed to measure displacement at the cutting tool in either axial or lateral directions and compare these displacements against the positions and controller setpoints of the corresponding machine axes. Additionally, a finite element model is created and expanded such that it emulates the machine encoders and additional cutting tool sensors, as well as the third order motion profile that is used to excite the system. Methods for automatically processing the data from these experiments and simulations are developed in parallel, allowing for large sets of data to be processed with little effort.

These experiments show that with a maximum amplitude of approximately 0.3 µm the vibrations that occur at the tool, relative to the axis encoder, are most significant in axial direction. A qualitative comparison with the finite element model indicates a mechanical issue relating to the Z axis drive mechanism, causing additional vibrations in the system. Finally, the experiment setups, corresponding data processing methods and finite element models are reflected on and incorporated into a framework for experimental machine performance evaluation. By implementing this framework, machine tool manufacturers can further evaluate and improve the dynamic performance of their machines.

1

Introduction

Throughout history lathes have been used to make a wide variety of objects by cutting material from a spinning workpiece. This started with softer materials, such as a wooden bowl in 1200 BC, progressing to harder materials, metal locomotive wheels in 1868 [1]. Aside from being able to cut harder materials, these machines were also being made more accurate, resulting in more accurate workpieces. An extreme example of this is the range of lathes produced by Hembrug Danobat, turning workpieces with a hardness of up to 70 HRC (Rockwell C, 1210 Vickers) with form and dimensional accuracies under 2 µm. These machines also produce a surface quality high enough to forego subsequent grinding operations. This increases productivity and workpiece accuracy while reducing cost and environmental impact [2].

A lathe is a machine that removes material from a rotating workpiece using a cutting tool. A schematic overview of the components of one of Hembrugs lathes is given in figure 1.1a. A steel frame (not shown in the figure) sits on the ground, on which a large granite base (8) is mounted using a set of vibration dampers (9). On the left, this is connected to a granite headstock (1), which contains the hydrostatic spindle (2). Attached to this spindle is the chuck, which holds the workpiece (3). On the right side of the granite base is the hydrostatic Z axis (7), of which the carriage can translate in the Z direction (shown in figure 1.1b). Mounted on the Z axis is the X axis (6), of which the carriage can translate in the X direction. Attached to this is a tool changer (5), which holds a series of cutting tools (4) that can be positioned to engage with the workpiece. As lathes often make axisymmetric parts, the movement directions are often referred to as axial (Z direction) and radial (X direction).

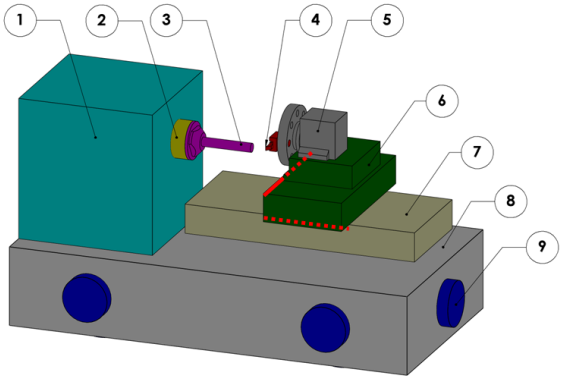

(a)

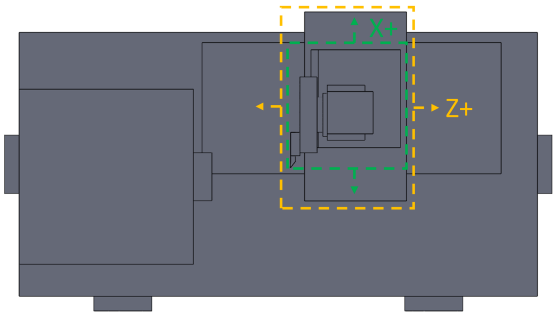

(b)

Figure 1.1: (a) Isometric overview of lathe components: 1) Headstock 2) Main spindle 3) Workpiece 4) Cutting tool 5) Toolchanger 6) X axis 7) Z axis 8) Granite base 9) Rubber vibration damper. X and Z linear encoders indicated by red lines (b) Top view of lathe movement directions: X (lateral) and Z (axial)

Aside from these mechanical components, the lathe also contains a set of electronic and electromechanical components. The X and Z axes are driven by servo motors. For both of these axes the position

is measured with a linear encoder, indicated in red in figure 1.1a, as well as a rotational encoder on the servo motor. These motors are in turn connected to their drivers, which receive commands from the numerical controller.

Even though these machines are already very accurate, vibrations are still present in the system and influence the cutting tool position, which in turn limits accuracy. In this thesis, the movement of the machine axes as a vibration source will be investigated. Vibrations in the Y direction will be omitted from this investigation, since any variation of the cutting tool position in Y direction, d_y, has negligible influence on the product diameter when compared to variations in the X direction, d_x. This is illustrated by figure 1.2.

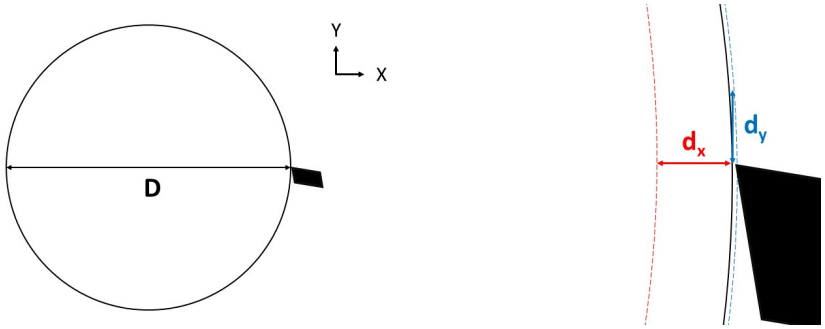

Figure 1.2: Influence of X and Y displacement on workpiece diameter

Several experiments and finite element models will be designed, made and executed specifically for this investigation. Together with the method of analysing the large amount of data that these experiments will yield, these experiments and finite element models will form the basis of a framework for experimental machine performance evaluation.

In the following chapter the theory of systems modelling, vibrations, vibration sources and motion profiles will be discussed. After this, the methodology of a series of experiments and numerical model simulations is introduced. The results of of these experiments and simulations will be presented and discussed, after which conclusions are drawn and recommendations for future research are made.

2

Theory

In this chapter, we will explore the theory required for modeling vibrations in a hydrostatic lathe, as well as the causes of inaccuracies in machining. We will begin by introducing the fundamental concepts of modeling dynamic systems, including eigenfrequencies and eigenmodes. As all the bearings in the system are hydrostatic, we will also discuss the basics of hydrostatic bearings. Next, we will examine the causes of inaccuracies in the workpiece produced by the machine. After this, we will discuss the forces typically present in a lathe and the causes of inaccuracies in the workpiece. Finally, the numerical controller and motion profile it generates will be introduced.

2.1. Machine model

2.1.1. Single DoF

The first step to modeling machine responses is to create a model that represents the structure. This model often shows the displacements that occur when the structure is subjected to a certain load. In its simplest form, a lathe can be approximated by a single degree of freedom (DoF) system, as shown in figure 2.1a.

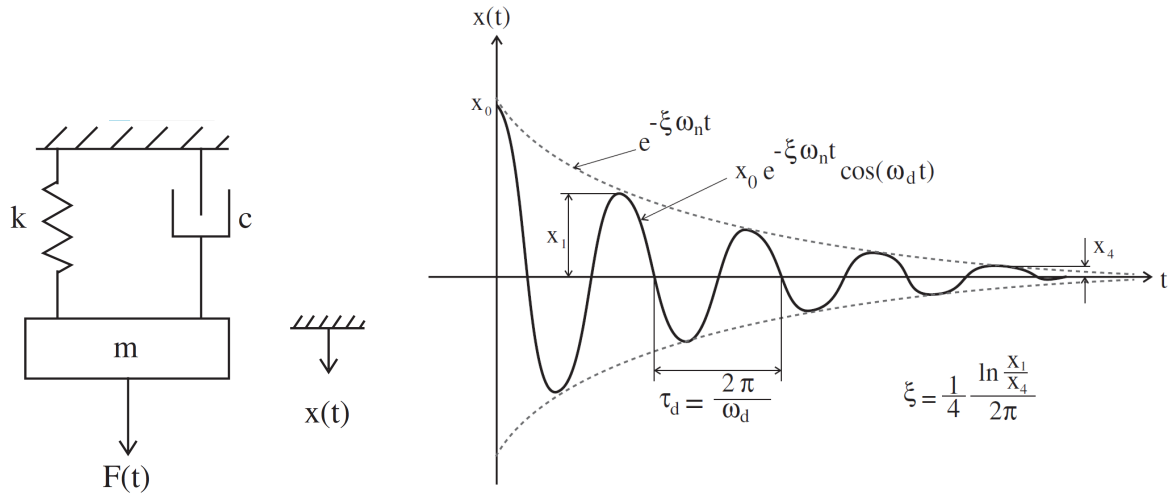

(a) Mass spring damper system

(b) Corresponding time response

Figure 2.1: Single degree of freedom mass spring damper system [3]

In this model mass m [kg], stiffness k [N/m] and damping coefficient c [Ns/m] are the model parameters. When a force F [N] is applied to the system, a deflection of x [m] occurs. When a displacement x_0 is applied to an underdamped system it will oscillate after being released, damping out over time. This is shown in figure 2.1b. In this figure ω_n [rad/s] is the natural frequency, ω_d [rad/s] is the damped natural

frequency, ζ [-] is the damping factor and τ_d [s] is the damping time. The damped natural frequency relates to the natural frequency and damping factor as follows [3]:

$$\omega_d = \omega_n\sqrt{1-\zeta^2}$$

The relationship between damping coefficient and damping factor is given by [3]:

$$c = 2m\zeta\omega_n$$

When introducing parameters velocity v [m/s] and acceleration a [m/s^2], the equation of motion for the system can be described [3]:

$$F = ma + cv + kx$$

It is also possible to represent the system in the frequency domain. To do this, a Fourier transform is applied to the equation of motion of the system. Rewriting the resulting equation as a fraction of two system variables results in a transfer function [3]. With a bode plot, this transfer function can be visualized. Figure 2.2 shows the bode plot of transfer function $X(j\omega)/F(j\omega)$ of a single DoF mass spring damper system, with a varying quality factor. The quality factor is yet another way of describing the damping properties of the system and relates to the damping factor as follows [4]:

$$Q = \frac{1}{2\zeta}$$

Using the bode plot one can see the difference in magnitude between the force and displacement for each frequency. It also clearly indicates the eigenfrequency at 10 Hz, as well as the phase delay for each frequency.

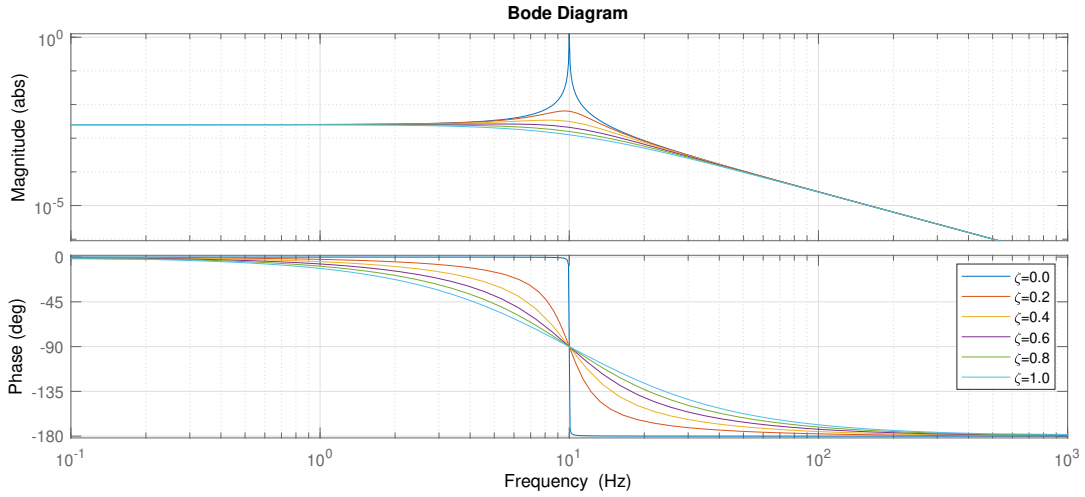

Figure 2.2: Bode diagram of a single DoF mass spring damper system for a range of damping factors

2.1.2. Multiple DoF

A single DoF model is useful for quick estimation of model dynamics, but only contains a single eigenfrequency. To study more complex systems, containing multiple eigenfrequencies, a multiple degree of freedom model is required. This can be done by adding multiple single DoF systems in series, as shown in figure 2.3a. A system with two mass spring damper sets has two eigenfrequencies and two corresponding eigenmodes. An eigenmode shows the magnitude and direction of each body when the structure vibrates with the eigenfrequency. An example of the modeshapes of a 2DoF system is shown in figure 2.3b. Fourier analysis, as introduced in the previous section, can also be applied to multiple DoF systems.

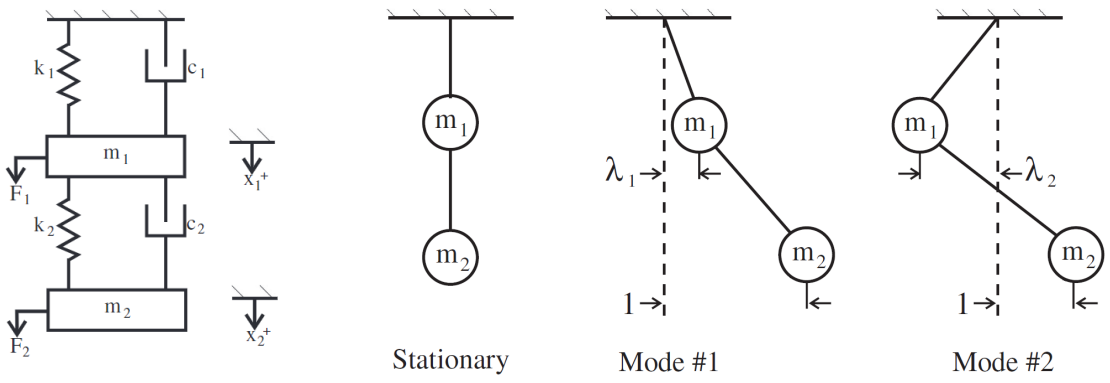

(a) Double mass spring damper system (b) Modeshapes of a double pendulum

Figure 2.3: Systems with two degrees of freedom, modified from [3]

2.2. Hydrostatics

The lathe that is the subject of this thesis uses hydrostatic bearings. Hydrostatic bearings are composed of two opposing bodies, separated by a continuous flow of pressurized fluid. Since there is no contact between the two bodies, the bearing surfaces do not wear over time. Another advantage of hydrostatic bearings is that there is no stick-slip effect, which allows for very precise positioning. [5]

A schematic overview of a circular hydrostatic thrust bearing is shown in figure 2.4. Pressurized fluid flows through a flow restrictor in the top body, into a cavity. From this cavity (recess) the fluid moves through a narrow gap between the bodies (bearing land), decreasing in pressure until it reaches ambient pressure. Rowe [5] explains how the out-of-plane stiffness, out-of-plane damping and in-plane damping can be calculated. All these depend on the recess dimensions, fluid film thickness, supply pressure, recess pressure and viscosity. It is important to note that hydrostatic bearings have no in-plane stiffness.

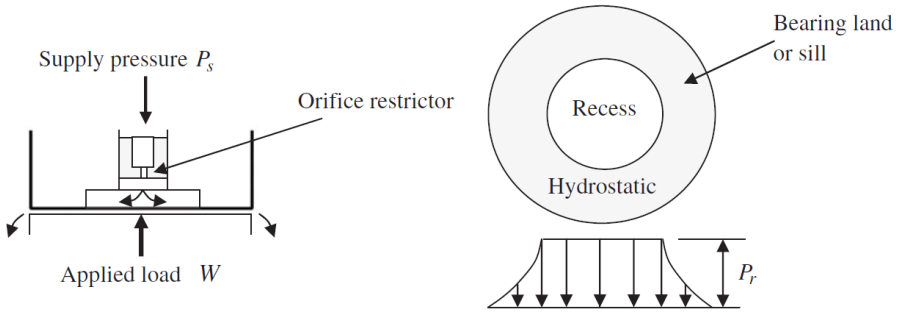

Figure 2.4: Cross section, bottom view and pressure distribution of a circular hydrostatic thrust bearing, modified from [5]

2.3. Vibrations

When vibrations are present in a machine structure, they may lead to undesired displacements during cutting. To understand how to mitigate their influence, it is first important to understand how these vibrations are generated. There are two types of vibrations that occur during cutting: free and forced vibrations. Furthermore, there are also self-excited vibrations, which are a special subset of forced vibrations [3].

2.3.1. Free vibrations

Free vibrations are vibrations that occur when a system is subjected to an impulse. The system starts oscillating around its steady state with the natural frequency. When damping is present, the oscillation dampens, until steady state is achieved. An example of this can be seen in figure 2.1b.

2.3.2. Forced vibrations
Forced vibrations are vibrations that occur when a system is subjected to a varying force, which displaces the system. If the system is underdamped it will vibrate.

2.3.3. Self-excited vibrations
Self-excited vibrations are vibrations that are caused by forces present in the system. For a cutting process, the most common self-excited vibration is chatter. Chatter occurs when the cutting tool of the system cuts with an inconsistent depth [3], which may occur at the beginning of a cutting process or when the tool encounters inhomogeneities in the material. This phenomenon is illustrated in figure 2.5 for a radial turning process.

To further illustrate this, imagine a perfectly smooth cylinder that is clamped in a lathe. A cutting tool approaches the material and starts a radial cut (as indicated with 'Feed Direction' in figure 2.5) with intended chip thickness h_0. When the cutting tool first engages the material it experiences an impulse, which results in a damped vibration of the cutting tool. The profile of this vibration depends on stiffness k_y and damping coefficient c_y. The periodic movement of the tool with respect to the workpiece results in a varying chip thickness $h(t)$, which in turn results in a wavy surface. After one spindle period T, the workpiece has made one revolution and the tool encounters the wavy surface $y(t-T)$. Depending on the phase shift ϵ between the previous and current revolution, the difference in chip thickness may increase. This behavior can cause poor surface finish, dimensional accuracy and tool life. [3]

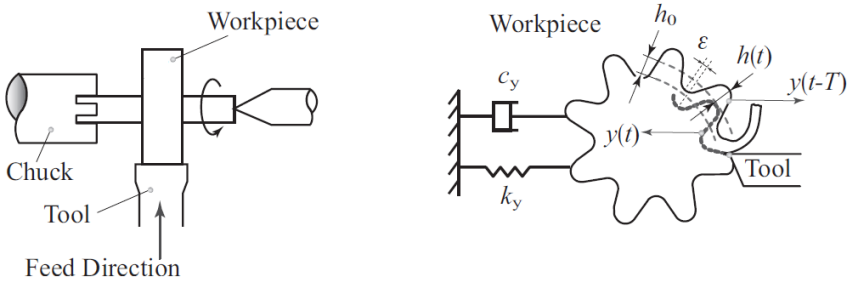

Figure 2.5: Self-excited vibrations in a radial turning operation, modified from [3]

2.4. Forces
In this section, we will investigate the sources of forces present in a machining system and how these forces affect the accuracy and quality of the workpiece.

2.4.1. Machine acceleration
When a structure is accelerated, it is subjected to a reaction force proportional to the acceleration. For the objective of this thesis, accelerations in the Z direction (parallel to the spindle axis) are dominant. With a combined weight of several hundreds of kilograms, the force at the Z carriage is in the order of 1 kN.

2.4.2. Cutting
Another source of forces in the structure is the cutting process. When the cutting tool is in contact with the workpiece, a contact force emerges at their interface. A schematic overview of the components of this force is shown in figure 2.6.

Altintas [3] describes how the components of the contact force can be calculated. These force components are called the feed, radial and tangential forces, and act in their respective directions. The contact force depends on tool geometry such as rake angles, relief angles and nose radius. It also depends on cutting parameters such as depth of cut, feed rate and cutting constants. These constants are empirically derived for various materials and cutting tools.

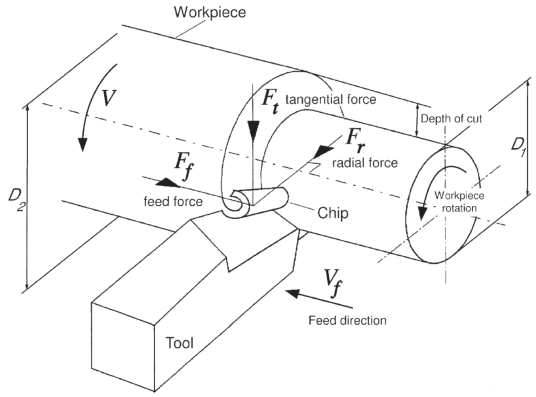

Figure 2.6: Cutting forces in a turning process [3]

A more general approach is found in the catalogs of tooling suppliers. This approach only yields the total contact force, but is a convenient alternative for quick calculations [6]:

$$F = k_c a_p f$$

For a general finishing operation with a depth of cut a_p of 0.05 mm, a feed rate f of 0.1 mm/rev and specific cutting force k_c of 4000 N/mm^2, the total contact force is 20 N. It should be noted that the units for this equation do not match, since the equation uses feed rate instead of chip thickness [mm]. Functionally, these two parameters indicate the same thing: the amount of material that is removed while cutting. The equation likely uses feed rate since this is parameter is directly used when programming the machine, which makes the information easier to understand for the average user.

2.5. Inaccuracies

To increase machine productivity, its accuracy must be increased. With higher accuracy, machine parameters can be adjusted, allowing for faster cycle times without sacrificing quality. Using the information provided in the previous sections, multiple sources of inaccuracies can be identified. These will be discussed below. Aside from these mechanical sources, the control system and setpoint generation software may also negatively influence the accuracy of the system. This is the topic of another research project that is being conducted simultaneously. As such, this will not be investigated in this thesis.

2.5.1. Deflection

Deflection can be split into two categories: Static and dynamic deflection. For two identical cuts, the static deflection will be equal. On the workpiece, this deflection results in an over- or undersized feature. This difference can then be compensated in the machine controller, allowing for the following workpiece to be unaffected by the static deflection [7].

Dynamic deflection occurs when vibrations are introduced in the system. These vibrations can originate from three sources: The machine surroundings, the machine movement (accelerations) and the tool-workpiece interaction [8]. As seen in chapter 1, the machine bed is made of granite, which is known for its vibration damping properties [9]. Additionally, the granite bed is mounted on vibration dampers, connected to the steel frame. Because of this, vibrations originating from the surroundings will be neglected. The remaining two sources do not necessarily have equal impact. To find out which has the greatest influence further investigation is required. This will be done in the following chapter.

2.5.2. Other sources

Aside from static and dynamic deflection, there are some process related sources. Since these highly depend on the specific process, they will not be investigated. Nevertheless, for completeness sake they are identified here.

First there is suboptimal cutting parameters. A cutting process depends on many parameters. Among these are rotational speed, cutting depth and feed rate. For each combination of material and cutting tool, there is a certain optimal range of these parameters. If the cutting happens outside of this

favorable range, worse results will be achieved. It is up to the user to choose the proper combination of these parameters. Therefore, the influence of cutting parameters will not be investigated in this thesis.

Secondly, there is tool wear. As the tool is cutting the material, the contact area is wearing. When the tool is worn far enough, its cutting behavior will deteriorate. To prevent problems due to tool wear, the tool needs to be replaced in time. This, too, is up to the user and as such, it will not be investigated.

Finally, there are vibrations that originate from the other side of the tool-workpiece contact. When the workpiece is thin walled or insufficiently clamped, it may start vibrating due to the tool-workpiece contact, which can lead to self-excited vibrations. Since these problems are again highly dependent on the specific workpiece and workholding, they will not be investigated.

2.6. Numerical controller

The lathe that is the subject of this thesis is equipped with a Siemens Sinumerik 840D sl numerical controller. A numerical controller (NC) takes positional commands and converts these in corresponding motion of the axes, as indicated in figure 2.7.

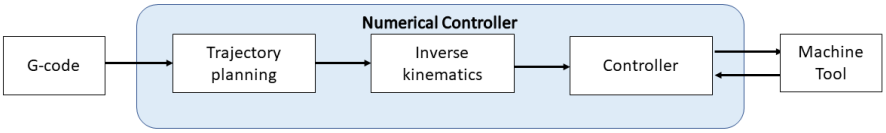

Figure 2.7: Overview of functions of numerical controller (NC)

The NC receives positional commands in the form of G-code as an input. These commands are then translated into a set of signals using trajectory planning. Trajectory planning is the generation of a set of signals that make the attached machine move along a certain path, given constraints such as position, velocity and acceleration [10]. After this, the desired motion of the end effector is translated into required motion of each of the axes using inverse kinematics. Finally, the signals are sent to the controller. The controller then drives the motors of the machine, ensuring that the trajectory is followed in a sufficiently accurate manner [10].

In the Sinumerik 840D sl numerical controller, the control system consists of three cascaded feedback loops, controlling position, velocity and motor current, respectively [11]. These are shown in figure 2.8. As the influence of settings of the NC are the subject of another research project, this thesis limits itself to the position control loop. As seen in the figure, the NC defines a position setpoint and the motor encoder provides the actual position. The difference between these two values is called the following error.

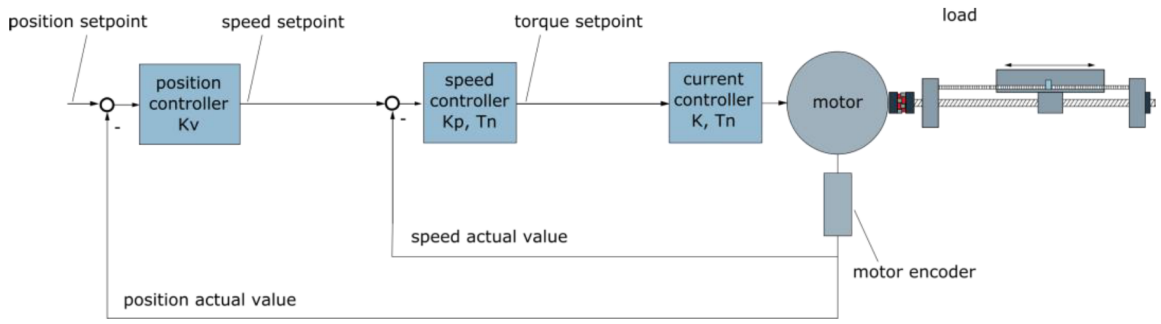

Figure 2.8: Sinumerik 840D sl control system [11]

In this thesis the position reported by the linear encoders will be evaluated alongside the position reported by a sensor at the tool. As such, the following error of the tool is defined as the difference between the actual tool position and the position setpoint. Note that this position setpoint is the same for the encoder and the tool positions. Figure 2.9 gives an overview of the Encoder Following Error (EFE), Tool Following Error (TFE) and Tool Dynamic Error (TDE), the latter of which is defined as the difference in position of the tool with respect to the encoder.

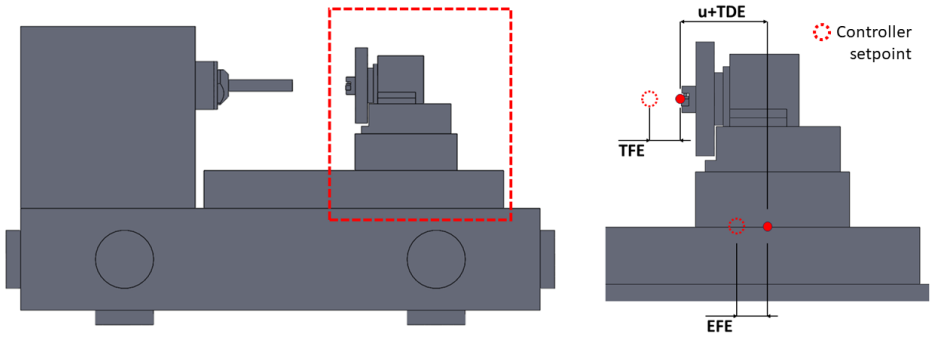

Figure 2.9: Schematic overview of Encoder Follow Error (EFE), Tool Following Error (TFE) and Tool Dynamic Error (TDE)

2.7. Third order point-to-point motion profile

As discussed in section 2.4.1 the movement of the machine axes can be used to excite the system and study the resulting vibrations. The movement of the lathe is described by a third order motion profile, which uses the third time derivative of position, jerk, as a basis. A point-to-point motion profile is a specific type of third order motion profile that describes movement between two points, with the boundary condition of standstill at both points. It is also possible to create third order motion profiles that pass through points at specified velocities and accelerations, but since boundary conditions of this type are not used in this thesis, they are not discussed.

An example of a third order motion profile is shown in figure 2.10. This profile is generated using a jerk value j =200 m/s^3, a maximum acceleration $a = 5$ m/s^2, a maximum velocity $v = 0.5$ m/s, and a desired displacement $s = 100$ mm. Whether or not the maximum values of acceleration and velocity are achieved during this motion profile depends on the specific values of the motion profile parameters. JPE [12] describes six types of third order point-to-point motion profiles and provides a systematic approach for determining which type is appropriate for a given set of parameters . This approach then yields a set of eight points in time. At each of these points, jerk becomes either zero or the positive or negative maximum value. Acceleration, velocity and position are then finally calculated for each timestep:

$$
\begin{aligned}
j_i &= \begin{cases} j_{\max} \\ 0 \\ -j_{\max} \end{cases} \\
a_i &= j_i(t - t_{i-1}) + a_{i-1} \\
v_i &= \frac{1}{2} j_i (t - t_{i-1})^2 + a_{i-1}(t - t_{i-1}) + v_{i-1} \\
x_i &= \frac{1}{6} j_i (t - t_{i-1})^3 + \frac{1}{2} a_{i-1}(t - t_{i-1})^2 + v_{i-1}(t - t_{i-1}) + x_{i-1}
\end{aligned}
$$

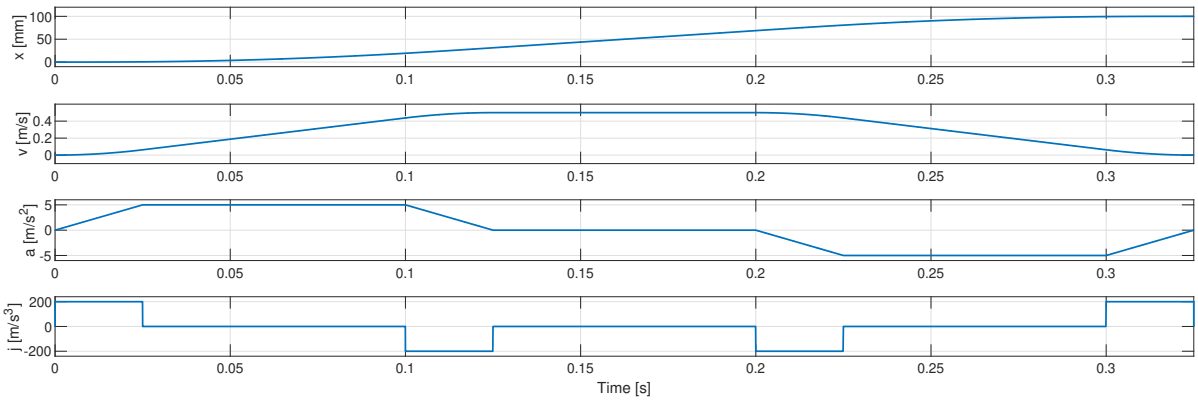

Figure 2.10: A third order point-to-point motion profile

3

Methodology

As described in the previous chapters, the goal of this thesis is to investigate vibrations occurring at the tool. In the following section, a comparison between two vibration sources is made to limit the scope of the thesis. After this, several experiments are designed, described and conducted. The first experiment provides parameters that are required to build a finite element model, the following experiments evaluate vibrations in the machine. Finally, a finite element model is created.

3.1. Determine influence of cutting forces

As discussed in the previous chapter, the influence of machine acceleration and tool-workpiece contact as vibration sources needs to be evaluated. To do this, a test is set up. The machine is run through a typical series of moves, axially (along Z) cutting a hardened metal workpiece, as indicated in figure 3.1. Using the linear encoder present in the Z axis of the machine, the Z position is measured with a sampling rate of 500 Hz. The Z following error, computed by the NC, is also saved. The workpiece is then removed and the series of moves is repeated. Figure 3.2 shows the following error of both tests for a single stroke of the Z axis, indicated in blue in figure 3.1.

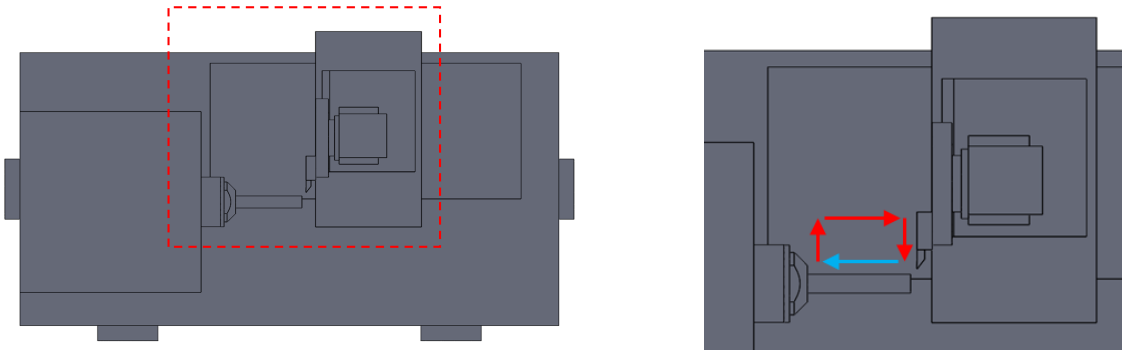

Figure 3.1: Schematic overview of machine movement

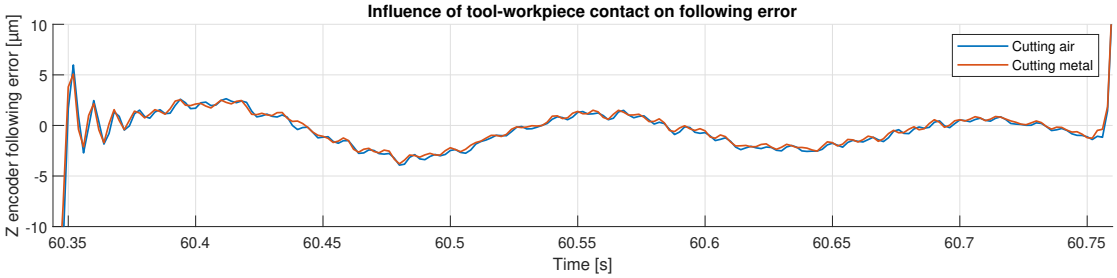

Figure 3.2: Influence of tool-workpiece contact on following error

As can be seen in the figure, the following error for both cycles is virtually identical. Since the only difference between the two cycles is the the material contact we can conclude that, for the current set of cutting parameters, any vibrations originating from tool-workpiece contact are not sensed at the sensor location. However, it cannot be concluded that this contact never influences the Z position error. A different set of cutting parameters might, for example, produce vibrations of a higher amplitude, allowing them to be sensed at the sensor position. It is also possible that any vibrations originating at the tool are not sensed because the eigenmode corresponding to this vibration does not excite the sensor position. A final option would be that the vibrations caused by the tool-workpiece contact have a frequency that is higher than the 250 Hz Nyquist sampling criterion for this measurement.

As discussed in the previous chapter, the influence of different cutting parameters will not be investigated, because finding an optimal set of cutting parameters is up to the user of the machine. The problem of eigenmodes and sensor locations, however, should be investigated further. Vermeulen [13] has done extensive research on the eigenfrequencies and modes found in this series of hydrostatic lathes. From this it can be seen that eigenmodes up to 200Hz can be sensed at the linear encoder. In figure 3.2, two distinct frequencies are observed. These frequencies can be calculated using the formulas shown in figure 2.1b. The slow vibration has a damped natural frequency of about 7 Hz, which is close to the rigid body mode of the system mounted on the vibration dampers. The fast vibration has a damped natural frequency of about 117 Hz, which is close to the axial resonance frequency of the Z-axis [13].

With the data that is currently available it is difficult to prove that the tool-workpiece contact has no influence on the workpiece. However, in experiments previously conducted at Hembrug, the same slow vibration that is seen in figure 3.2 was observed in the measured workpiece. This gives sufficient reason to further investigate these vibrations. With this, we can infer that vibrations originating from machine acceleration have a greater influence on following error than those from tool-workpiece contact.

3.2. Damping factor of rubber elements

In this thesis a finite element model of the machine will be created. To correctly implement the machine characteristics in this model, its elements must be properly defined. The stiffness and damping factors of the rubber elements that connect the granite bed and machine base determine the rigid body mode of the machine. The axial and lateral stiffness of these rubber elements is given in the datasheet, but for the damping factor this is not the case. This information is required for the machine model and will be experimentally determined in this section.

Figures 3.3a and 3.3b show the overall test setup, which was specifically designed and fabricated for this test. A rubber element is bolted to a steel base, which is placed on a granite surface plate. An aluminum housing is then bolted to the top of the rubber element. A PCB Piezotronics 356A16 triaxial acceleration sensor magnetically attaches to the bolt that connects the housing to the rubber element. Finally, an aluminum lid is affixed to the aluminum housing. The three acceleration signals are then fed into a Data Translation DT9837A data acquisition system, which samples the data a 50 kHz, after which the data is logged in MATLAB. The housing is then lightly struck with a small hammer, three times in each of the sensors sensing directions, as indicated in figure 3.3b.

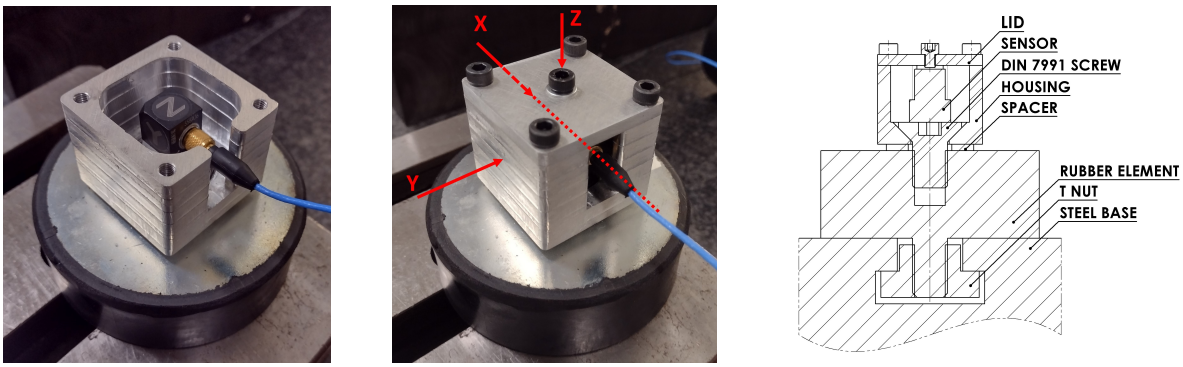

(a) Sensor and housing (50x50x40mm) mounted on rubber element

(b) Lid mounted on housing and actuation directions

(c) Section view of experiment setup

Figure 3.3: Damping factor test setup

The test is repeated with a steel flange mounted in between the sensor housing and rubber element. This is done to investigate the influence of additional mass on the damping factors. Both of these tests are finally repeated on two identical rubber elements.

The experiments result in six datasets: three for the tests without additional mass and three or the tests with additional mass. Each dataset contains the X, Y and Z direction acceleration data that resulted from hitting the housing 9 times. These responses are automatically isolated and filtered to reduce the influence of additional vibrations that likely resulted from a decrease in contact stiffness between the aluminum housing and rubber element. This decrease is likely a result of galling and improper tightening. Figure 3.4a is an example of a normal impulse response. Figure 3.4b is an example of impulse response with undesired additional vibrations: A high frequency vibration during the first 10 ms, and a beating pattern influencing the slow vibration.

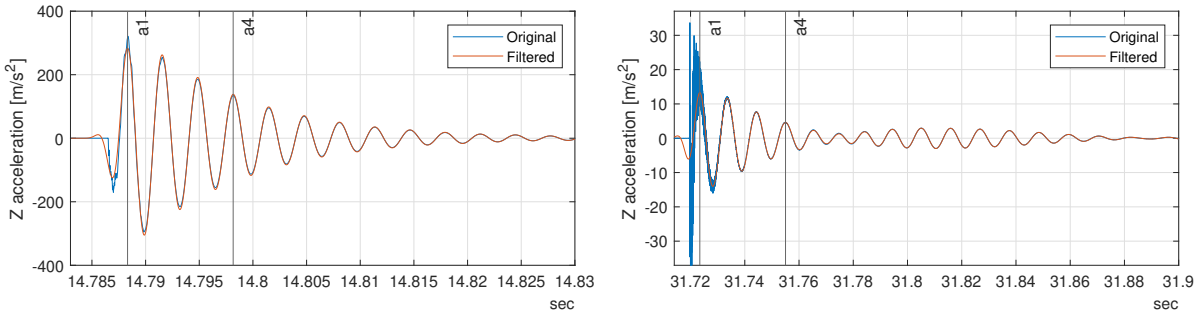

Figure 3.4: (a) Z direction impulse response 3 without additional mass - containing very slight undesired additional vibrations (b) Z direction impulse response 1 with additional mass - containing beating and undesired additional vibrations

After the impulses of all datasets are isolated, they are restructured into 6 new datasets, as described by table 3.1. Each dataset now contains 9 impulse responses, all measured in a single direction. For each dataset impulse responses 1-3 are taken from the first rubber element, 4-6 from the second and 7-9 from the third. An overview of all impulse responses can be found in appendix A.

Table 3.1: Restructured datasets

	X direction	Y direction	Z direction
Without additional mass	dataset 1	dataset 2	dataset 3
With additional mass	dataset 4	dataset 5	dataset 6

For each impulse response, the amplitudes of the first (a_1) and fourth (a_4) peak are automatically found. The damping factor is then calculated for each impulse response:

$$\zeta = \frac{1}{4}\frac{1}{2\pi}\ln\frac{a_1}{a_4}$$

Note that this equation is analogous to the equation shown in figure 2.1b.

The damping factors calculated from acceleration data in X and Y directions are the lateral damping factors. The Z direction acceleration data give the axial damping factor. In total, there are 36 impulse responses that are used to calculate the mean lateral damping factor and 18 impulse responses that are used to calculate the mean axial damping factor. These are shown in figure 3.5.

As can be seen in the figure, lateral damping factors 7-9 and axial damping factors 1-6, all with added mass, differ significantly from the rest. For all axial damping factors with additional mass, this is because these signals all contain beating. The decay in amplitude of the impulse response differs due to this beating pattern. For impulse responses 7-9 the beating amplitude is small and likely results in very little error.

The damping ratio could still be found for the signals that contain beating. One approach would be to fit a general sinusoidal beating pattern to each of the responses. While feasible, this approach would require additional coding and is computationally expensive. Since there is a sufficient amount of impulse responses that do not contain beating, these damping factors will be ignored.

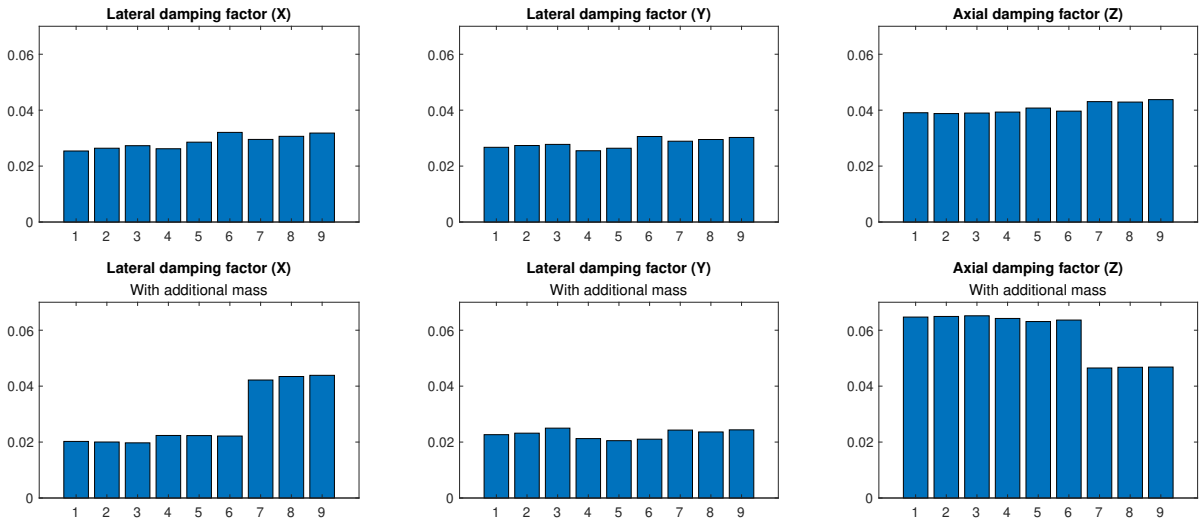

Figure 3.5: Lateral and axial damping factors for each impulse response

With this information, we can calculate the average damping factors: $\zeta_l = 0.026$ and $\zeta_a = 0.042$ for the lateral and axial direction, respectively.

3.3. In-machine measurements with additional sensors

To further investigate the relationship between vibrations measured at the linear encoder and those occurring at the tool, two additional tests are designed. For each test, the position and following error are measured using the linear encoders. An additional sensor then measures the relative distance between the tool and the spindle, in Z and X direction respectively. The system is excited by moving the carriage with a third order motion profile in the Z direction. The combination of these datasets allows for analysis of the relationship between vibrations at the encoder and tool for a variety of third-order motion profiles. The range of maximum acceleration and jerk settings are indicated in table 3.2. As reported in this table, a jerk value of *Brisk* is used for three of the datasets. *Brisk* is a setting in the NC that forces acceleration without jerk limitation [14]. The jerk values in the table were chosen in such a way that for each acceleration setting the low and medium jerk setpoints result in a motion profile that is 10% and 2% slower than the motion profile with *Brisk*.

Table 3.2: Controller settings for each dynamic motion profile

Dataset	2	3	4	5	6	7	8	9	10
Acceleration [m/s^2]	1.2	1.2	1.2	2.5	2.5	2.5	4	4	4
Jerk [m/s^3]	20	100	Brisk	55	275	Brisk	100	500	Brisk

Note that dataset 1 is not included in this table; this is a quasistatic movement that is used to compensate for any systematic error present in the system. The system is then set up with an additional sensor for each test, which will be discussed in the following sections.

3.3.1. Laser interferometer (Z)

The Z-direction vibrations occurring at the tool are measured using a laser interferometer. The laser interferometer measures distance to a moving object by analyzing the interference pattern resulting from two light beams that reflect off the moving and a stationary object respectively [15].

Measuring displacement using a laser interferometer is often done to evaluate the quasistatic behavior of the machine axes and find geometric errors that can then be compensated using the NC [16]. The same methods can be applied to analyse the dynamic behaviour of the system. [17] directly measures vertical displacement of the spindle of a milling machine during cutting. [18] analyses displacement, velocity and acceleration of a milling machine table for various commanded velocities.

Both of these examples analyse signals obtained using a single measurement method. To gain

insight in how vibrations at the tool relate to vibrations measured at the axis encoders, signals from two measurement systems must be compared. In [19] the dynamic positioning accuracy of a coordinate measuring machine is investigated, comparing the position reported by the axis encoder to the position of the end effector reported by the laser interferometer. A similar approach is taken in this thesis.

The test setup uses a Renishaw XL-80 laser interferometer. Combined with an XC-80 compensator, which compensates for environmental influences such as temperature and humidity, the laser interferometer has a sampling rate of 50 kHz, a resolution of 1 nm and a measurement accuracy of ±0.5 ppm (0.05 µm over a distance of 100 mm) [20]. Figure 3.6 shows the general setup for this test. The XL-80 interferometer is mounted on a tripod outside of the machine, the XC-80 and its sensors are mounted inside the machine. The beamsplitter and first reflector are mounted on the headstock and the second reflector is mounted in the tool changer. The mounts for the beamsplitter and both reflectors were designed to allow for adjustment. As can be seen in the figure, each component location can be adjusted to ensure proper alignment. The headstock components can be adjusted in Y and the toolchanger components in X. Finally, the tripod that the laser interferometer is mounted to can be adjusted in all six degrees of freedom.

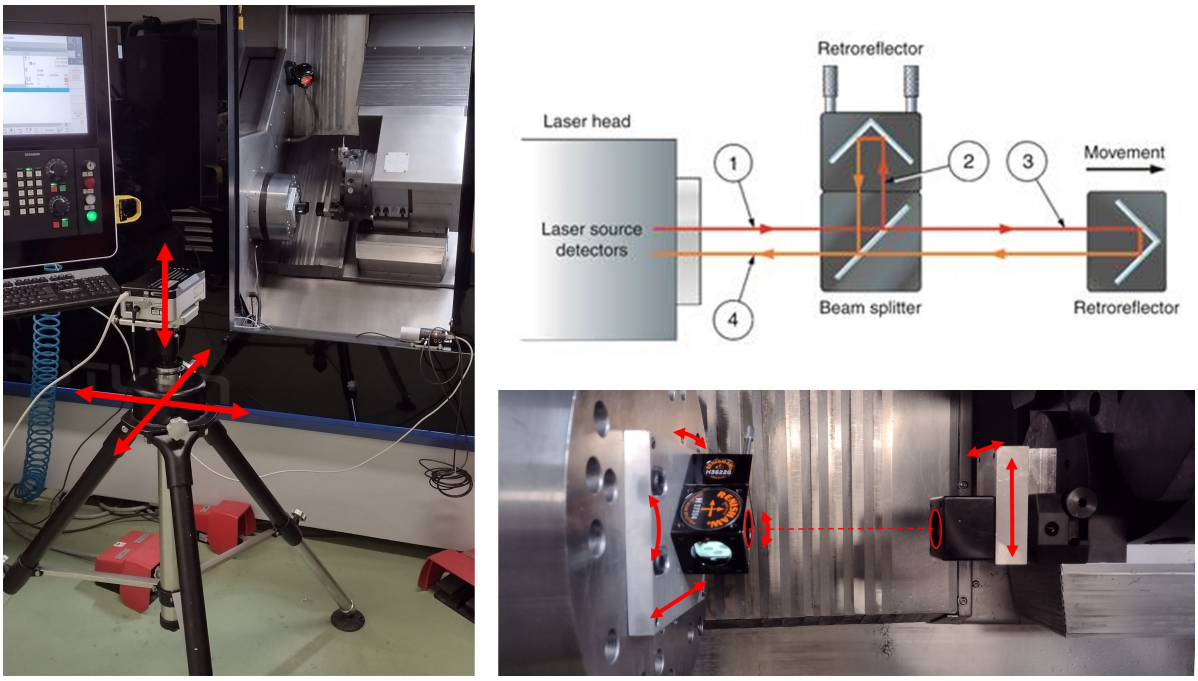

Figure 3.6: (a) Tripod adjustability (rotations not shown) (b) Laser interferometer components and layout for a linear measurement [15] (c) Beamsplitter and retroreflectors adjustability

When the measurement setup is complete and carefully aligned, the Z axis is moved with a third order motion profile, after which it repositions for the following stroke. Figure 3.7 shows the analysed movement direction in blue and the repositioning movements in red. This is repeated for various combinations of maximum jerk and acceleration. The position datasets captured by the linear encoder and laser interferometer are then post-processed and analyzed. The results of these analyses will be discussed in the following chapter.

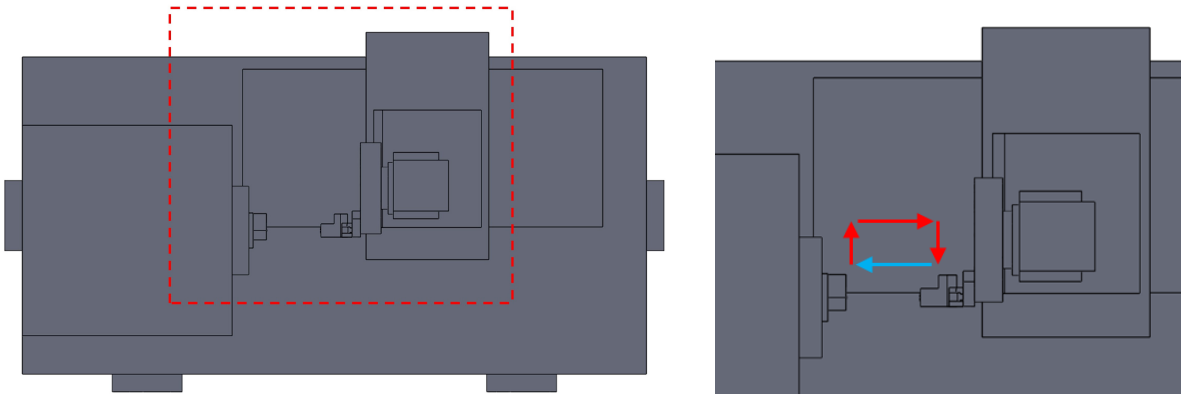

Figure 3.7: Z direction experiment movement

3.3.2. Capacitive sensor (X)

The X-direction vibrations occurring at the tool are measured using a capacitive distance sensor. Similar to the laser interferometer, this measurement method is often applied to quasistatically find geometric errors of slide assemblies [16, 21]. For this experiment, it will be applied during dynamic movements. Figure 3.8 shows the measurement setup.

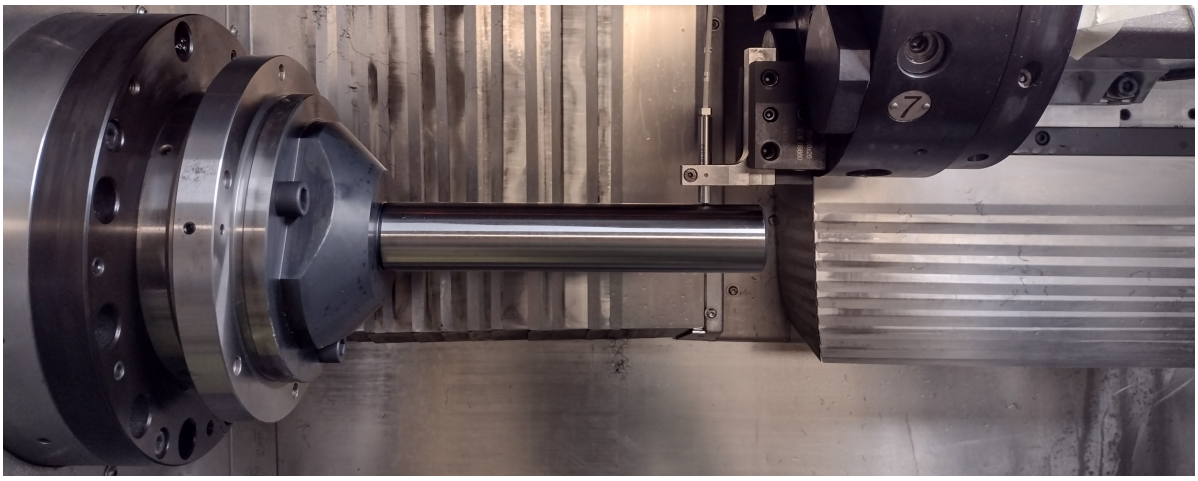

Figure 3.8: X-direction test measurement setup

A ground shaft is mounted on the flange of the spindle and adjusted such that the total indicated runout is under 2 µm. The mount for the capacitive sensor ensures that it is aligned in X and is positioned sufficiently close to the shaft.

The signal from the Lion Precision C7-C capacitive sensor with 80 mV/µm sensitivity [22] is read by MATLAB using a Lion Precision DMT22 driver with a maximum full scale linearity error of $\pm$ 0.3% [23] and a Data Translation DT9867A dynamic system analyser with a 24 bit resolution.

Three quasistatic measurements over the measurement range are first taken to compensate for any errors in parallelism to the Z axis and straightness of the shaft surface. Afterwards, the system is again excited using a third order motion profile in the Z direction, after which it returns to its start position. Figure 3.9 shows these movement directions in blue and red, respectively. With these datasets it is possible to investigate the vibrations occurring at the tool in X direction. The results of these analyses will be discussed in the following chapter.

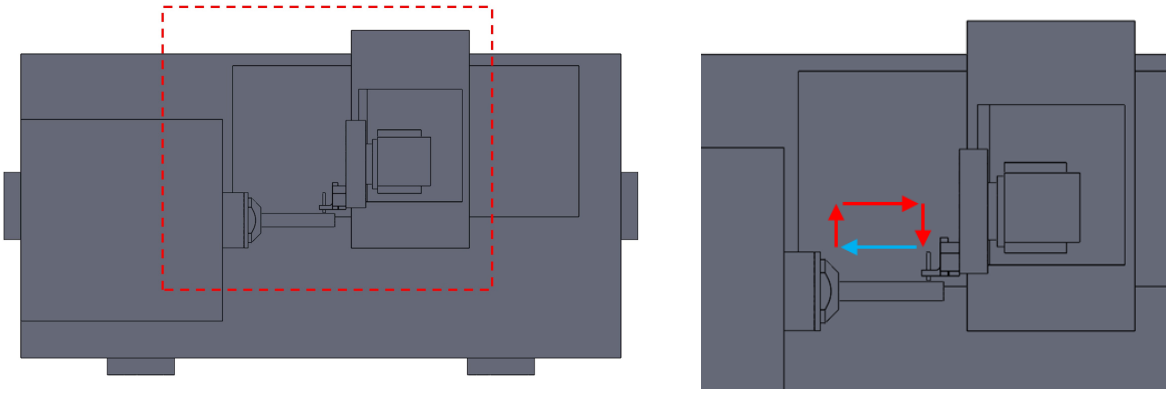

Figure 3.9: X direction experiment movement

3.4. Finite element model

Now that the experiments described in sections 3.3.1 and 3.3.2 have been performed, a finite element model can be made and subsequently be validated using the experiment results. In this section we will first discuss the general setup of the model in COMSOL Multiphysics 6.0, after which we will explain how each test setup will be modelled.

3.4.1. General model setup

In the following sections multiple studies will be described. Each study is based on the same general model. To make the geometry of the finite element model, a detailed CAD model of the machine is stripped of all elements that do not influence vibrations that can be measured at the tool, such as the outer sheetmetal, which is decoupled from the machine. Certain aspects of the model are then simplified to decrease mesh size. Each simplification is considered regarding its expected influence on model accuracy. After these changes the model is imported into COMSOL.

The studies that will be performed are solid mechanics studies in the time and frequency domain. The setup for these studies varies slightly, but the majority is identical:

- A spring foundation for the rubber elements, set up with stiffness and damping in all local directions.
- A thin elastic layer for the hydrostatic bearings, with stiffness in local Z and X directions; Z for the hydrostatics, X for the ballscrew stiffness.
- Correct material properties for the steel and granite components.
- A free tetrahedral mesh, split into several sections to reduce mesh size, shown in figure 3.10.

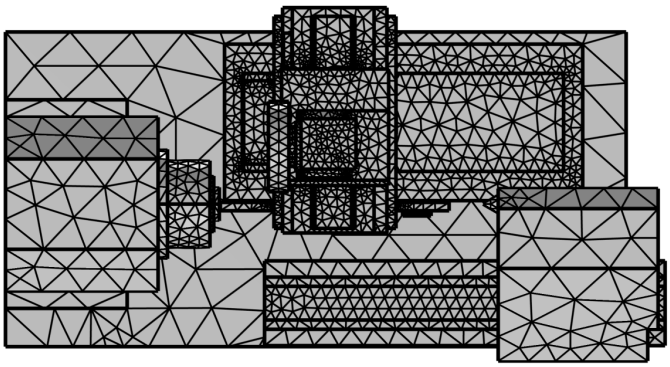

Figure 3.10: Mesh applied to general model

3.4.2. Damping coefficient

COMSOL requires a damping coefficient to include damping in time-dependent studies. In section 3.2 the axial and lateral damping factors were experimentally determined. Additional work is required to obtain the damping coefficients from the damping factors.

As discussed in section 2.1.1, for a single DoF system the damping factor and coefficient are related through the mass and eigenfrequency of the system. However, the current system contains multiple dampers in multiple orientations. Furthermore, as discussed in section 3.2, the axial and lateral damping factors are not identical. To obtain the correct corresponding damping coefficients, a parameter sweep is set up in COMSOL.

First, the damping of the spring foundation that represents the rubber elements is set up with axial and lateral loss factors η_a and η_l.

$$\boldsymbol{\eta} = \begin{bmatrix} \eta_l & 0 & 0 \\ 0 & \eta_l & 0 \\ 0 & 0 & \eta_a \end{bmatrix} = 2 \begin{bmatrix} \zeta_l & 0 & 0 \\ 0 & \zeta_l & 0 \\ 0 & 0 & \zeta_a \end{bmatrix}$$

The quality factors corresponding to the first six eigenfrequencies are then saved and the rubber elements are set up with viscous damping:

$$\boldsymbol{c} = \begin{bmatrix} c_l & 0 & 0 \\ 0 & c_l & 0 \\ 0 & 0 & c_a \end{bmatrix}$$

Factors p_l and p_a are applied to c_l and c_a respectively and are automatically varied over a series of studies using a parametric sweep. The first iteration starts with $\boldsymbol{c} = 2m\boldsymbol{\zeta}\omega_n/16$, which is the relation between the damping factor and damping coefficient introduced in section 2.1.1, adjusted for the number of effective dampers. For this calculation, m and ω_n are found using the loss factor study. For each combination of p_l and p_a, the quality factors corresponding to the first six eigenfrequencies are again saved. The full dataset of factor combinations and corresponding quality factors is exported to MATLAB, where the six-dimensional euclidean distance is calculated between the goal quality factors and each set of quality factors obtained from the parametric sweep. Figure 3.11 shows the found optimum. First, the optimum of available combinations is calculated, after which a quadratic fit is made through the closest points, finding the optimum.

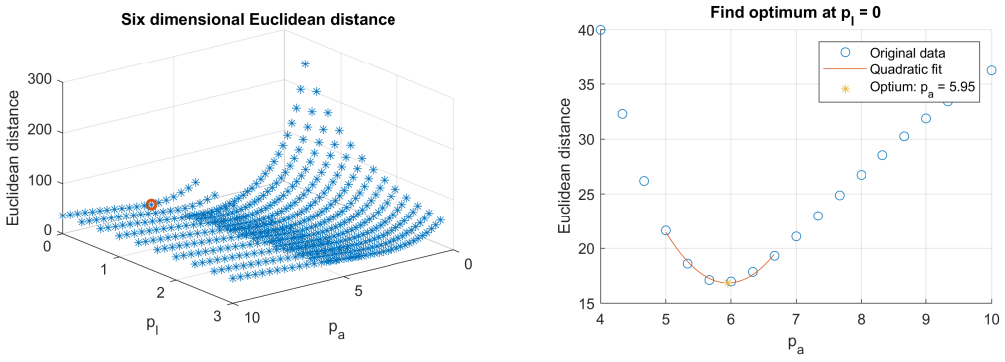

Figure 3.11: Finding the optimum combination of p_l and p_a

With this, $c_l = 0$ Ns/m and $c_a = 2760$ Ns/m. It should be noted that the lateral damping coefficient fits best when at zero. This likely means that for the given configuration of rubber elements, mechanical structure and excitation direction, the eigenmodes of the structure are not in a direction that is influenced by the lateral damping coefficient.

3.4.3. Time-dependent study

Now that the damping coefficients are found, the time-dependent study is set up. As mentioned earlier, the setup is similar to that of the previous studies. In the previous section, the Z-axis ballscrew stiffness was implemented as a thin elastic layer, acting between the interfaces of the hydrostatic bearing. In

reality, the reaction forces of the axial stiffness should not be applied at the hydrostatic interfaces, but at the nut (mounted on the Z-axis carriage) and thrust bearing (mounted on steel, attached to the granite bed).

In the following section the ballscrew stiffness will be applied correctly. It will be set up such that it allows for prescribed Z-axis displacement, identical to the displacement used to excite the system in sections 3.3.1 and 3.3.2, while still transferring forces that would result from additional displacement.

When evaluating the positions of certain nodes of interest over time, this position is reported with respect to a global coordinate system. As the granite bed moves through space when excited by the prescribed motion profile, the global X and Z directions do not align with the X and Z axes of the machine. The implementation of a local coordinate system is discussed afterwards.

Ballscrew stiffness while allowing prescribed movement

First, the Z-axis ballscrew stiffness is removed from the study, replacing it with virtual stiffness k [N/m], that acts on the nut mounting and thrust bearing faces, indicated by numbers 1 and 2 in figure 3.12, respectively. COMSOL function *aveop* is used to evaluate the average X, Y and Z coordinates of these faces for each point in time. With these coordinates, the euclidean distance between the faces at the start of the simulation, d_0 [m], as well as the distance at each of the subsequent timesteps, d_i [m], is calculated. Using the desired Z-axis location d_{act} [m], the force applied to the nut and thrust bearing faces is defined as:

$$F = (d_{act} + d_i - d_0)k$$

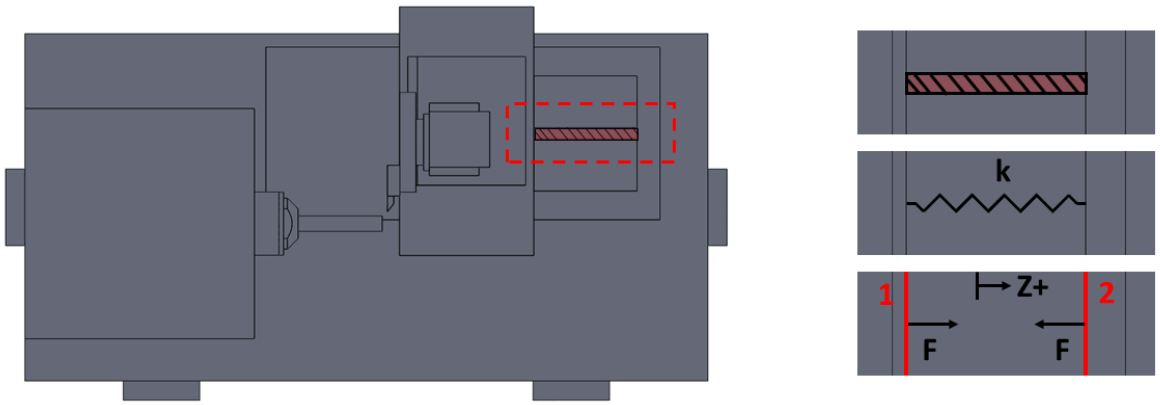

Figure 3.12: Z-axis axial stiffness diagram

As discussed in section 2.7, the shape of a third order motion profile depends on each of the motion profile parameters j, a, v and s. The approach described in this section is converted into a MATLAB script. For a given set of parameters, this script provides the correct trajectory shape, points in time t_0 through t_7 and maximum jerk value.

The formulas described in section 2.7 are implemented in COMSOL. Then, variable d_{act} is created by combining the displacements of each section of the motion profile, as described in section 2.7:

$$d_{act} = \sum_{i=1}^{7} x_i$$

Finally, the setting *steps taken by solver* is set to *strict* so that the time-dependent solver is forced to report values at each timestep of the study, instead of allowing it to interpolate between timesteps.

Local coordinate system

In the experiments described in section 3.3, the relative X and Z displacement between two components is measured. This is also the goal of the finite element model. To do this, one could simply evaluate the displacement of relevant nodes over time. The issue with this approach is that the displacement is calculated with respect to a fixed coordinate system. When a force is applied to the machine, each of

the rubber elements is displaced. This displacement contains rotational elements. As such, the X and Z axes of the machine no longer match the global coordinate system in which the points are evaluated.

To account for this arbitrary displacement, a local coordinate system is defined. To do this, the positions of three nodes on the top face of the granite, indicated in figure 3.13, are evaluated over time, together with the nodes that need to be evaluated with respect to the local coordinate system. This data is then exported to MATLAB. First, two vectors are created between the bottom left node and the two other nodes, indicating the local Z and X directions. After normalizing these vectors, the cross product between these vectors gives the local Y direction. Each node of interest is then expressed in the local coordinate system by subtracting the global location of the local origin and taking the dot product of the resulting vector with the local X, Y and Z axes.

Note that the local coordinate system is orthonormal in the undeformed configuration. Although each of the vectors will have unit length at each timestep, they are not necessarily orthogonal to each other, since the body they are defined on deforms over time. The error in nonorthogonality will be discussed in chapter 5.

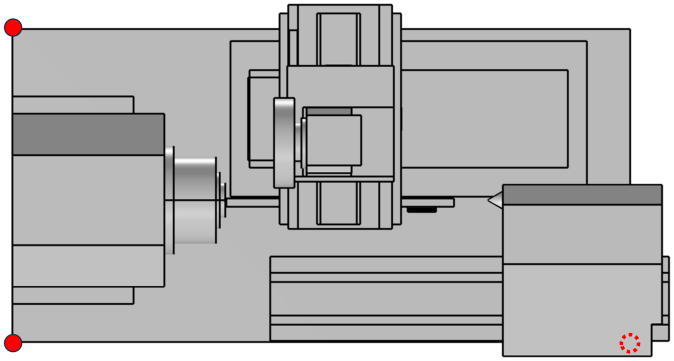

Figure 3.13: Nodes for local coordinate system

3.4.4. Simulation configurations

Now that the general finite element model has been set up, it can be adjusted to reflect both experiments that were conducted in section 3.3.

Laser interferometer (Z)

First, the model is adjusted and configured to match the test conducted in Z-direction with the laser interferometer. The beamsplitter and reflector are added, as well as the flanges and tool holder that are used to mount these on the machine. Then, the positions of the Z and X axes are adjusted to match the experimental setup. Finally, the motion profile parameters are adjusted to match the experiment.

The study is then executed. The positions of the beamsplitter and reflector are exported together with the nodes that define the local coordinate system and Z- and X-axis linear encoders. The results will be discussed in the following chapter. Figure 3.14 shows the geometry of the Z direction simulation finite element model.

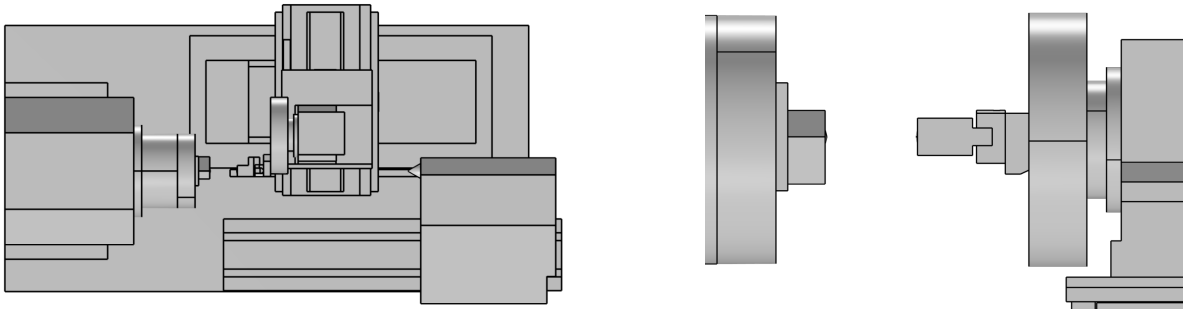

Figure 3.14: Laser interferometer configuration of the FEA model

Capacitive sensor (X)
Additional work is required to match the model to the experiment conducted in X-direction with the capacitive sensor. The model can quickly be expanded with the capacitive sensor and corresponding mount, but correctly implementing the ground shaft requires some more work. In the previous simulation, all movement was evaluated by evaluating nodes. However, in this simulation the relative displacement between the front face of the capacitive sensor and diameter of the ground shaft must be evaluated. Simply evaluating a node on the diameter of the shaft that is close to the sensor at the start of the simulation would result in these nodes moving apart as the simulation progresses. Since the shaft is a relatively long cantilever, the displacement along different positions of the shaft would likely vary significantly.

To circumvent this problem, a different approach is used to analyse the relative X-direction displacement between the ground shaft and capacitive sensor. First, the positions of the X and Z slides are again adjusted to match the start position of the experiment. In the experiment a slight air gap exists between the shaft and sensor. In the simulation, the X axis is adjusted so that these faces touch. A thin elastic layer with a stiffness of 1×10^{-15} N/m is applied to the boundary between these faces, which allows the bodies to move through each other while experiencing only negligible contact forces. The boundary between these two faces can then be evaluated using COMSOLs *up* and *down* functions. With this, the displacement orthogonal to the boundary can be evaluated for both bodies individually as the sensor moves along the length of the shaft.

Figure 3.15 shows the geometry of the X direction simulation FEA model. The results will be discussed in the following chapter.

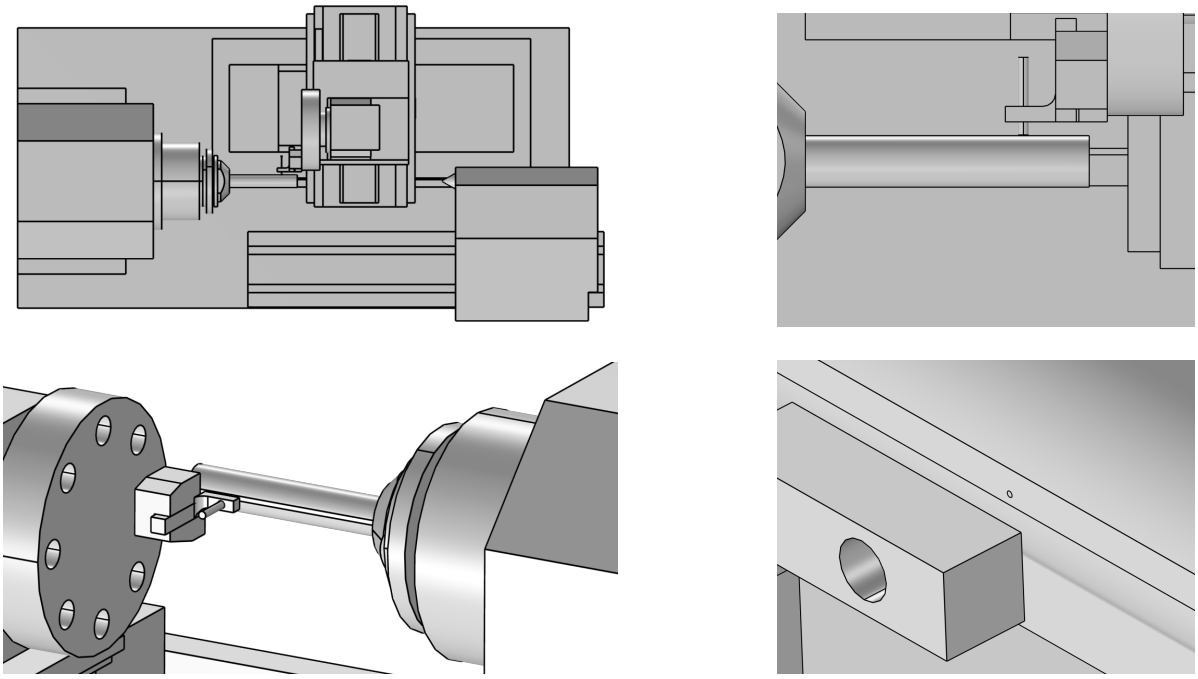

Figure 3.15: Capacitive sensor configuration of the FEA model. Second row: Interface between capacitive sensor and shaft

4

Results

In the previous chapter the experimental setup and simulation model have been discussed. In this chapter, the results of these experiments and simulations are presented. These are split up in two sections. The first section covers a comparison of the experiments and simulations for a single motion profile. The second section covers a comparison the results of the experiments of all 9 datasets.

4.1. Comparison of experiment and simulation results

This section covers the comparison of the results of the experiments and simulations of dataset 10, which has the highest jerk and acceleration values of all datasets, making it the fastest motion profile. This dataset has a motion profile with a movement of 100 mm, velocity 18 m/min, acceleration 4 m/s^2 and jerk setting of *Brisk*. As described in section 3.3, this means that the NC does not apply jerk limiting to the acceleration signal. For the simulation, a value of 400 m/s^3 is implemented. As will be shown in this chapter, this is approximately 10% lower than the actual jerk value for this dataset.

First, the Z direction experiment and simulation results are presented and compared. After this, the same is done for the X direction experimental and simulation results.

4.1.1. Z Experiment

As described in section 3.3.1, the Z axis movement is repeated multiple times for multiple motion profiles. First, the z axis is moved quasistatically. This measurement is repeated three times. The difference between the desired position (logged by the controller) and the position that the laser interferometer reports is shown in figure 4.1. This difference can be the result of various effects, such as a difference in machine temperature compared to when the internal machine compensation table was created. The mean quasistatic error is used to compensate the datasets of all following motion profiles.

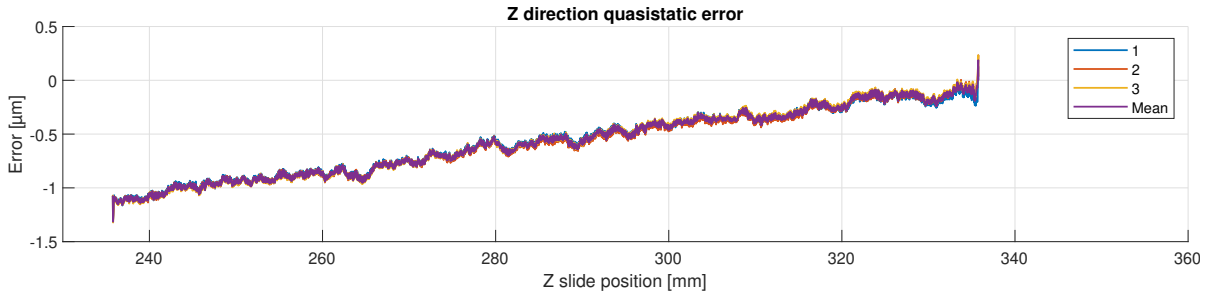

Figure 4.1: Quasistatic error of laser interferometer

After the quasistatic motion profile, the dynamic motion profiles are analysed. Each motion profile is repeated 10 times. Similar to the method used for analysing the data from the rubber elements, each instance is identified and analysed separately.

One of the main goals for this experiment is to quantify the difference (if any) between the position measured at the encoder and the position measured at the tool. Figure 4.2 shows the encoder and

tool positions, the encoder velocity, the tool and encoder following errors and the difference between the encoder and tool position.

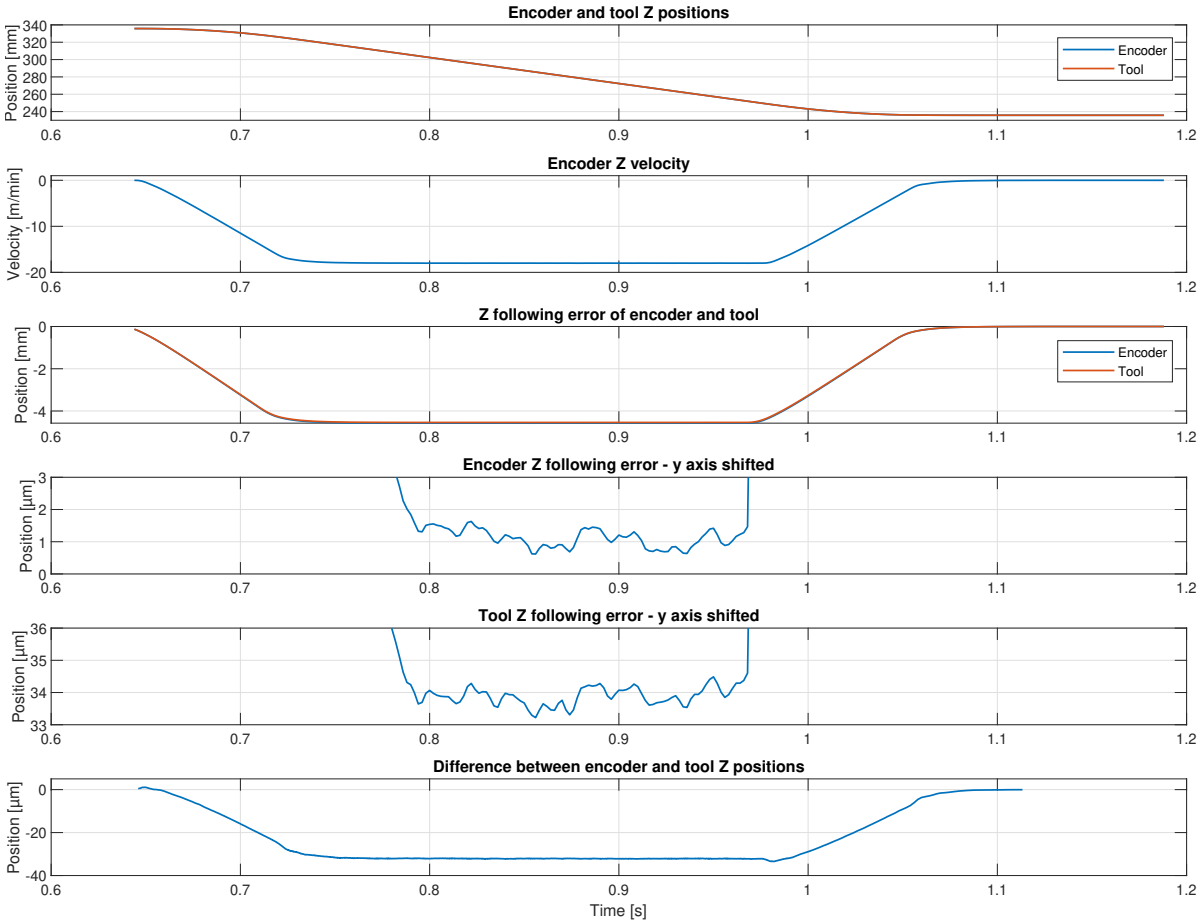

Figure 4.2: Overview of Z direction experiment

As can be seen in this figure, the following error is close to constant for a portion of time during constant velocity. Several frequencies can be found by counting the number of peaks that occur in a certain portion of time, analogous to the method shown in section 2.1.1. These frequencies are 14, 47 and 100 Hz for both the encoder and tool following errors.

From the last subfigure, one could conclude that during acceleration the tool starts lagging behind the carriage, reaching a constant lag when velocity is also constant. However, it is very unlikely that any dynamic displacement of the tool would contain this little visible vibrations while having such a large magnitude. Furthermore, as can be seen in the figure, the lag plot resembles the velocity plot. With a 500 Hz sampling rate the machine controller has a maximum of 0.002 s for all operations. During this time, the Z axis continues moving. There is a difference between the recorded time value and the actual time value of the exact moment the position values are logged. For comparison of signals measured by the controller this influence may be small. This is not the case for the comparison of signals of two measurement systems. When overlaying the encoder and tool Z positions, a delay of around 0.1 ms is observed. To properly align these signals, suppose that $f(t)$ is the tool position as measured by the laser interferometer, $g(t+\Delta t)$ is the encoder Z position, shifted by delay Δt and $g'(t+\Delta t)$ the first time derivative of $g(t+\Delta t)$. A first order Taylor expansion of the encoder position gives:

$$g(t) = g(t+\Delta t) - g'(t+\Delta t)\Delta t$$

The difference between the tool and encoder positions is then given by:

$$f(t) - g(t) = f(t) - g(t+\Delta t) + g'(t+\Delta t)\Delta t$$

This difference is the Z direction tool dynamic error. Note that this approach removes not only the delay caused by a delay in the controller, but also removes all delay caused by the mechanical system. Figure 4.3a shows the tool dynamic error together with the Z axis acceleration profile. This shows that the tool dynamic error aligns very well with the acceleration profile. Combined with the mass of the moving part of the system, the acceleration generates a body load. This displaces the tool. When acceleration returns to zero, the velocity is constant and only free vibrations remain. Figure 4.3b shows the range in time where velocity is constant.

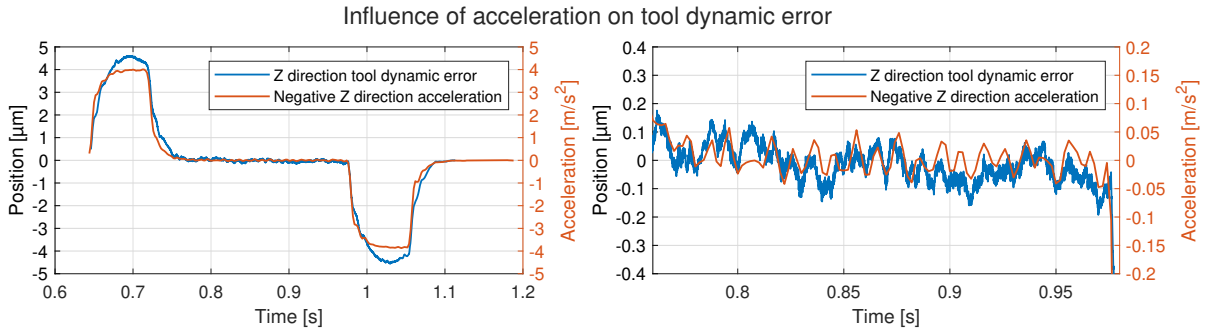

Figure 4.3: Comparison of acceleration and tool dynamic error (a) Complete (b) Constant velocity

In figure 4.3b two distinct vibrations of 14 and 100 Hz are found by manually counting peaks in the signal, as shown in section 2.1.1. The 100 Hz vibration is also visible in the acceleration signal. These frequencies should also be visible when analysing these signals in the frequency domain using the Fourier transform. Depending on the time range that is used for these Fourier transforms, frequency information of different parts of the signal is obtained. The bode plot of a Fourier transform of the signals shown in figure 4.3a is shown in figure 4.4, which shows a slight peak at 14 Hz, but no clear peak at 100 Hz. For both frequencies, neighboring peaks are equally prominent.

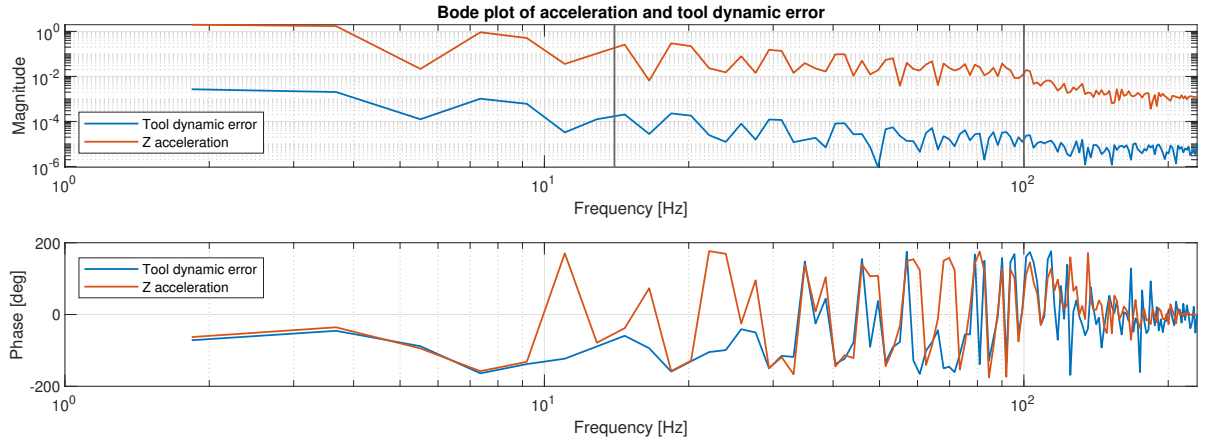

Figure 4.4: Bode plot of signals in figure 4.3a, vertical lines at 14 and 100 Hz

The bode plot of a Fourier transform of the signals shown in figure 4.3b is shown in figure 4.5. Here no clear peak is observed for 14 Hz, but at 100 Hz a peak is clearly visible. A bode plot of the Fourier transforms of the signal from the whole dataset, containing all 10 strokes, is shown in figure 4.6. All three figures contain vertical lines as markers at 14 and 100 Hz. As can be seen in these figures, a longer range in time creates a more defined bode plot but also contains frequency information of other time ranges, obscuring the desired frequencies. At the same time, frequencies that are prominent in the less-defined bode plot in figure 4.5 are not quite as distinct in the other two figures. This will be discussed further in chapter 5.

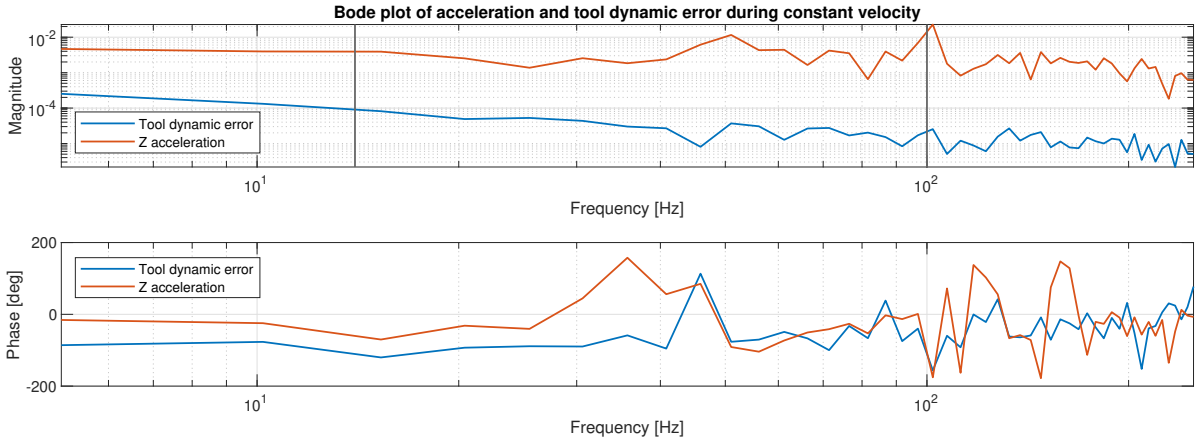

Figure 4.5: Bode plot of signals in figure 4.3b, markers at 14 and 100 Hz

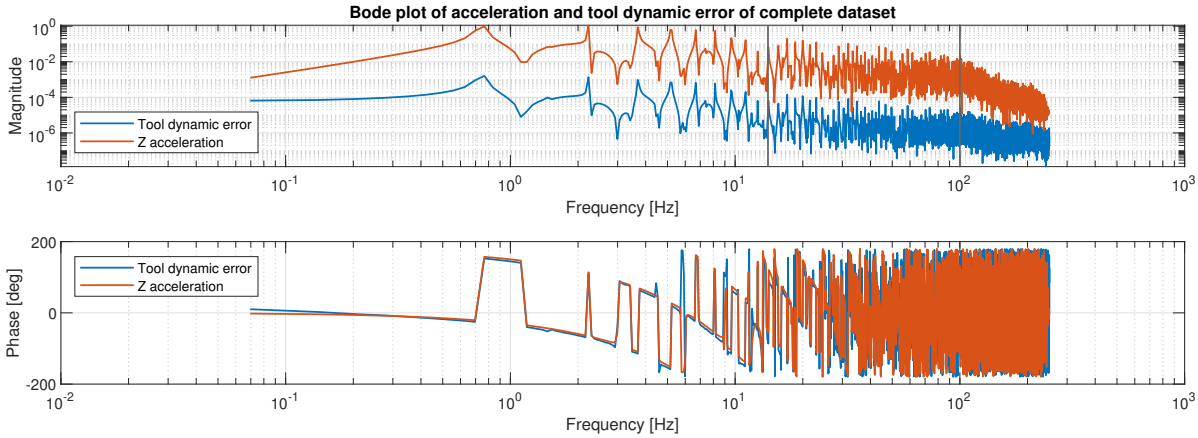

Figure 4.6: Bode plot of full acceleration and tool dynamic error datasets, markers at 14 and 100 Hz

4.1.2. Z Simulation

As described in section 3.4 the simulation model is adjusted to have the same geometry as the Z direction experiment. The same motion profile is used to excite the system and various nodes are evaluated over time, which are used to recreate the signals shown in the previous subsection. Figure 4.7 shows an overview of the simulation results. The first subplot shows the motion profile that was used to drive the Z axis.

The second subplot shows the difference between the encoder location and input motion profile, which is the following error of the encoder. As described by Vermeulen [13], the bandwidth of the Z axis controller is 40 Hz. This means that, depending on the vibration frequency, the controller can compensate for the low frequency vibration, but is unable to compensate the high frequency vibration. Filtering the encoder signal with a low pass filter with a cutoff frequency of 40 Hz yields the signal that can be compensated by the controller, shown in red.

The third subplot shows the difference between the tool location and input motion profile, which is the following error at the tool. The subplot shows the same behaviour as the encoder following error, only with a different amplitude.

The fourth subplot shows the Z direction tool dynamic error. This is the tool following error, compensated with the filtered encoder following error. This should resemble the tool dynamic error that would occur at the tool, if all frequencies lower than the controller bandwidth would be compensated by the controller.

In the Z direction tool dynamic error, two distinct frequencies can again be found by counting the number of peaks in a range in time: 6.5 and 106 Hz. Analogous to the analysis of the Z direction experiment, the Fourier transform of the tool dynamic error is taken. The bode plot of this signal is shown in figure 4.8 for the full stroke. Figure 4.9 shows the bode plot of the constant-velocity portion of the

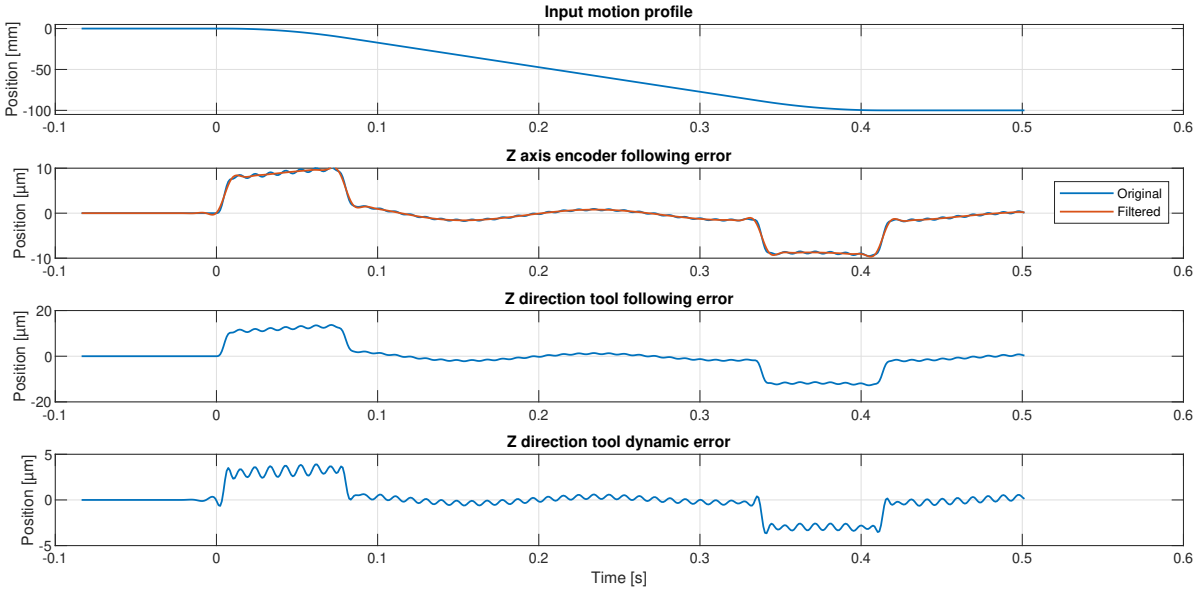

Figure 4.7: Z direction simulation results

signal. Analogous to the bode plots of the Z direction experiment, the single stroke bode plot contains more frequency information than the constant-velocity bode plot, but obscures the relevant frequencies. Both figures contain markers at the aforementioned frequencies. The bode plot of constant velocity tool dynamic error clearly shows a peak at 106 Hz.

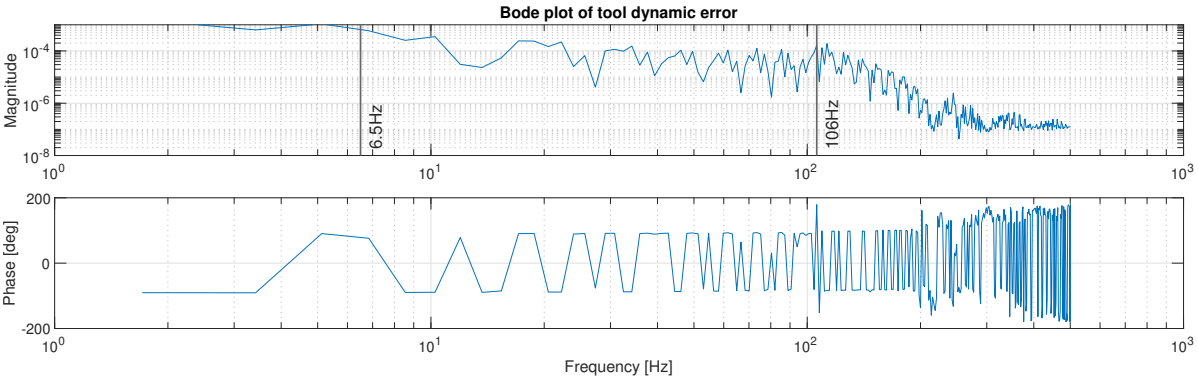

Figure 4.8: Bode plot of simulated tool dynamic error, markers at 6.5 and 106 Hz

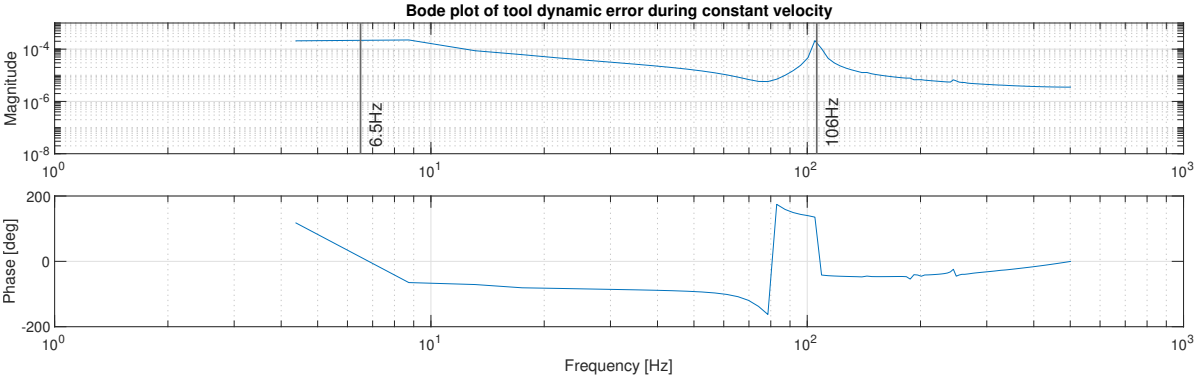

Figure 4.9: Bode plot of simulated tool dynamic error during constant velocity, markers at 6.5 and 106 Hz

4.1.3. Z Comparison

Now that the experiment and simulation results have been discussed, they can be overlaid to see how well they match. When the experimental and simulated Z direction tool dynamic error are overlaid, figure 4.10 is created. This figure shows that the overall shape of the signals matches quite well, but that the frequencies and corresponding amplitudes of the simulated tool dynamic error do not match. An overview of the frequencies found in the experiment and simulation is shown in table 4.1. The reasons for the differences in amplitude and frequency will be discussed in chapter 5.

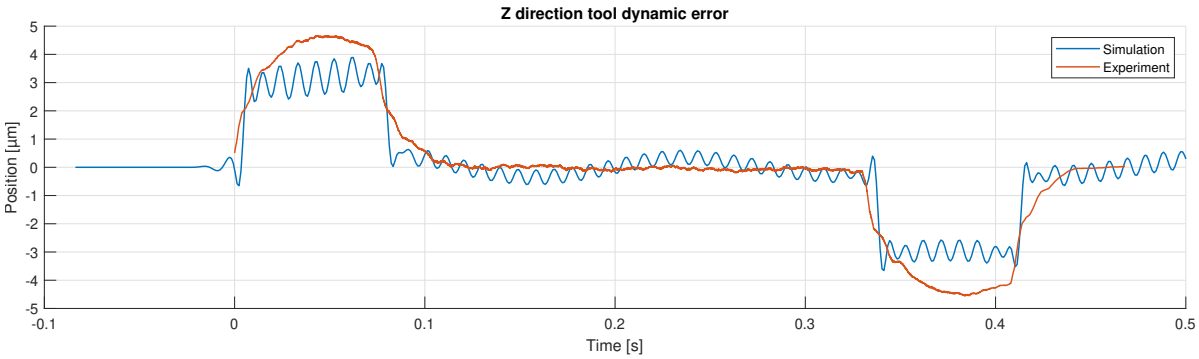

Figure 4.10: Comparison of Z direction tool dynamic error

Table 4.1: Comparison of frequencies found in experiments and simulations [Hz]

	Experiment			Simulation	
Z	14	47	100	6.5	106

The frequency domain results of the experiment and simulation can also be overlaid. This is done in figures 4.11 and 4.12 for a full stroke and during constant velocity, respectively. While both figures indicate that the magnitude of the experiment and simulation generally matches well, the latter figure also clearly indicates a difference in damping between the experiment and simulation, as the peak at resonance frequency is significantly more prominent. Additionally, the simulation bode plots are generally better defined, as these simulations contain no noise and have a higher sampling rate.

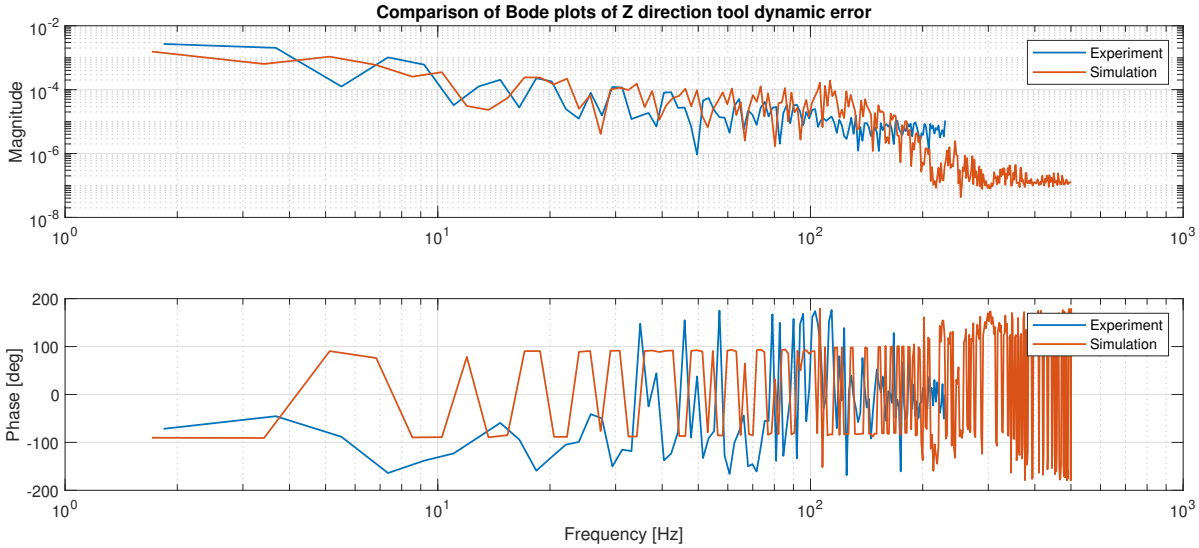

Figure 4.11: Bode plots of experiment and simulation results of Z direction tool dynamic error

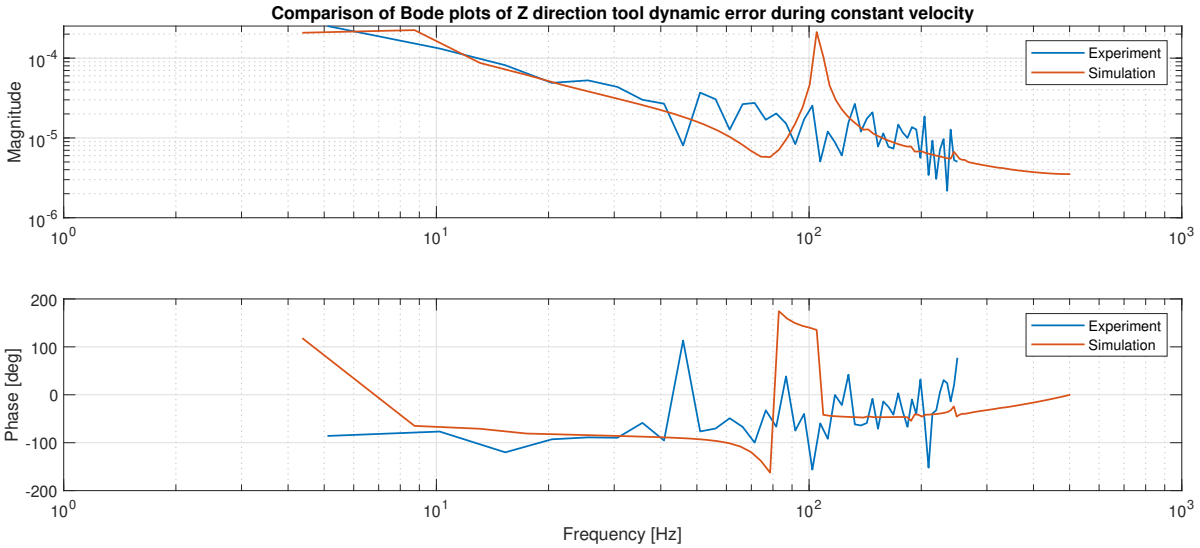

Figure 4.12: Bode plots of experiment and simulation results of Z direction tool dynamic error during constant velocity

4.1.4. X Experiment

Before the high acceleration movements are started, once again a set of three quasistatic Z direction movements is done. This gives a mean quasistatic error for both the X encoder and the capacitive sensor, shown in figure 4.13. It should be noted that even though only a Z direction command is issued, the X axis also moves at the encoder, which means that the controller is actively moving the X axis along with the Z axis. This is most likely the result of a compensation table that compensates for nonperpendicularity of the Z and X axis over the Z axis stroke.

Analogous to the Z direction analysis, these mean quasistatic errors will be used to compensate all dynamic datasets.

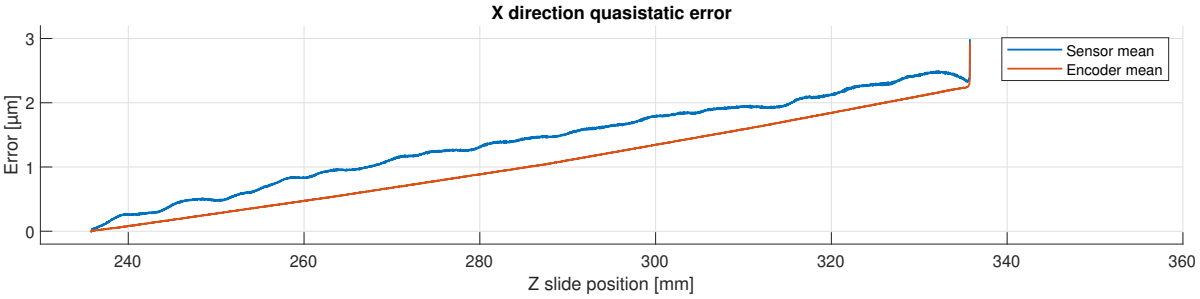

Figure 4.13: Quasistatic error

Once again, each dynamic motion profile is repeated ten times. The individual strokes are then isolated and analysed. An overview of this analysis is shown in figure 4.14. The first subplot shows the Z encoder position. The second subplot shows the X encoder, compensated for the quasistatic error shown in figure 4.13. This shows that the X axis moves 0.5 µm during this movement. The third subplot shows the capacitive sensor reading. Similar to the Z direction analysis, two peaks are visible, with an amplitude of around 0.5 µm. Note that the tool displacement during acceleration is not present at the encoder.

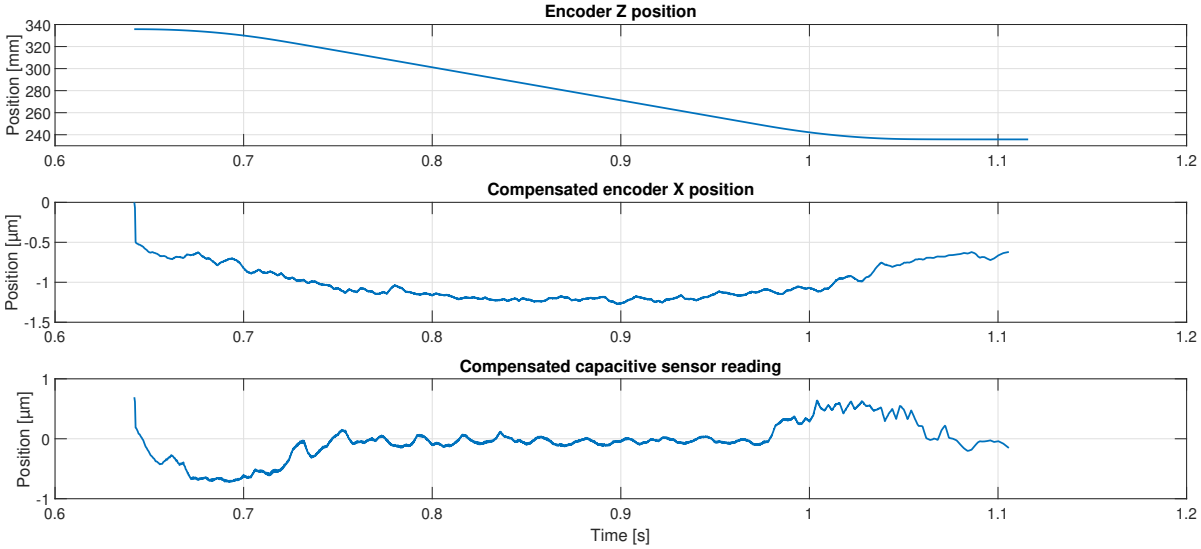

Figure 4.14: Overview of X direction experiment

In contrast to the Z direction analysis, the analysis of the X direction does not require any additional postprocessing, aside from changing the sign of the compensated sensor reading. This position signal can then be plotted together with the Z direction acceleration. This is shown in figure 4.15a. Figure 4.15b again zooms in on the part of the signal where velocity is constant.

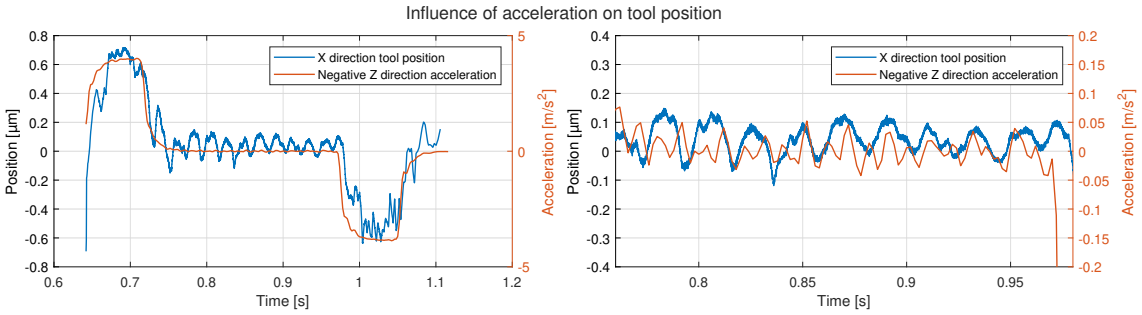

Figure 4.15: Comparison of acceleration and tool position (a) Complete (b) Constant velocity

The signals in figure 4.15b are manually analysed by counting the number of peaks visible in a given time, as described in section 2.1.1. The Z axis acceleration signal again contains a 100 Hz frequency. A 47 Hz frequency is present in the tool position signal. A higher frequency vibration, superimposed on the 47 Hz vibration, is visible as well and has a frequency of 160 Hz.

Taking the Fourier transform of the X direction tool position and Z direction acceleration for the ranges shown in figures 4.15a and 4.15b, the bode plots shown in figures 4.16 and 4.17 are created. Similar to the Z direction analysis the bode plot of the whole range of the signal, shown in figure 4.16, contains many frequencies, but none that clearly stand out. For the range where velocity is constant, shown in figure 4.17, a peak in the tool position bode plot is visible at 47 Hz. Small peaks are also visible at 100 and 160 Hz, though neighboring peaks are of similar magnitude. Again, the implications of this will be discussed in chapter 5.

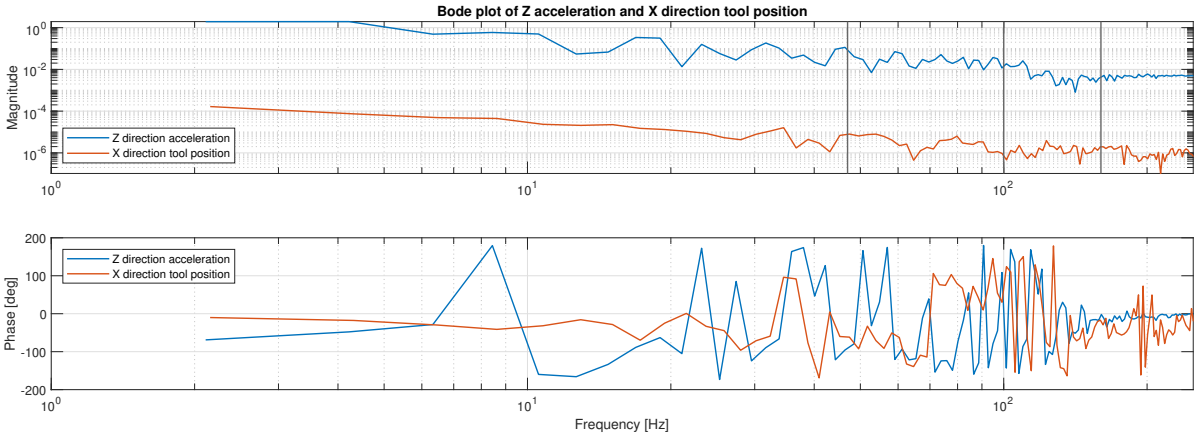

Figure 4.16: Comparison of bode plots of Z axis acceleration and X direction tool position, markers at 47, 100 and 160 Hz

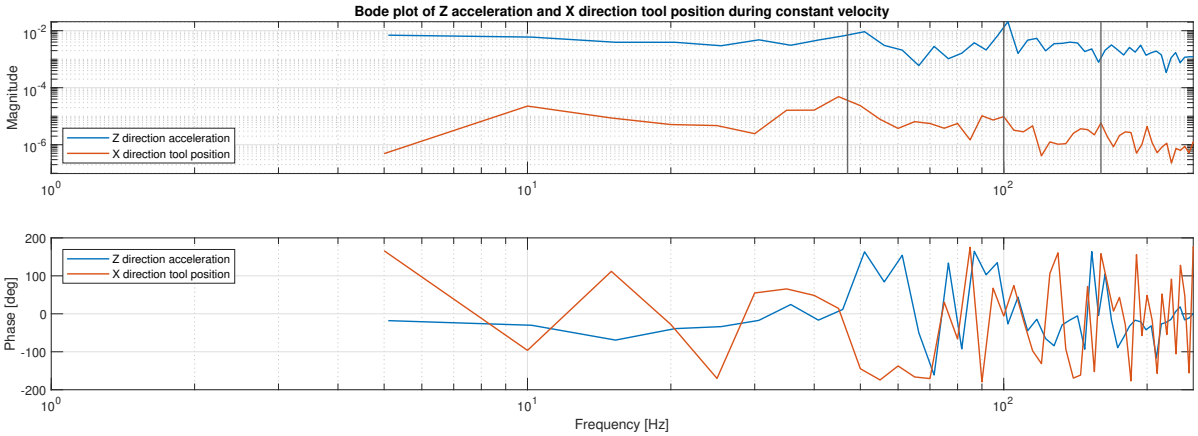

Figure 4.17: Comparison of bode plots of Z axis acceleration and X direction tool position during constant velocity, markers at 47, 100 and 160 Hz

4.1.5. X Simulation

Analogous to the Z direction simulation, the FEA model geometry is adjusted to match the experiment geometry. The same motion profile is provided as an input. When the simulation is finished, the coordinates of the relevant nodes are exported along with the motion profile and surface evaluation of the sensor boundary, so that they can be analysed.

Figure 4.18 shows the relevant information of this analysis. The first subplot shows the input motion profile. The second subplot shows the displacement of the X axis encoder. Once again, a 40Hz low pass filter is applied to the signal. This is the signal that the controller would be able to compensate. The third subplot shows the difference between the surface evaluations of the capacitive sensor interface. This is the X position of the tool. Note that in these subplots the positive directions are already aligned such that a positive value indicates a displacement in the positive direction. Finally, the fourth subplot shows the X direction tool position that resembles what would occur if the controller would compensate the filtered signal shown in the second subplot.

Several frequencies are clearly visible in the signals shown in subplots 2 through 4 of figure 4.18. Firstly, a vibration of 5 Hz is observed in the constant velocity part of the encoder position. For the tool position, a similar vibration with a frequency of 6.5 Hz is visible. As the compensated tool position is the difference between these two signals, this contains both frequencies. Aside from the low frequency vibrations, a 144 Hz vibration is also visible in all three signals. Finally, a beating pattern is visible only in the range in which accelerations occur. This pattern has a beat frequency of 35 Hz.

Figure 4.19 shows the bode plot of the Fourier transform of the compensated X direction tool position. Figure 4.20 shows this for the range in time where velocity is constant. In these figures no clear peaks are observed at 5 and 6.5 Hz. This is again likely due to the low resolution of the Fourier

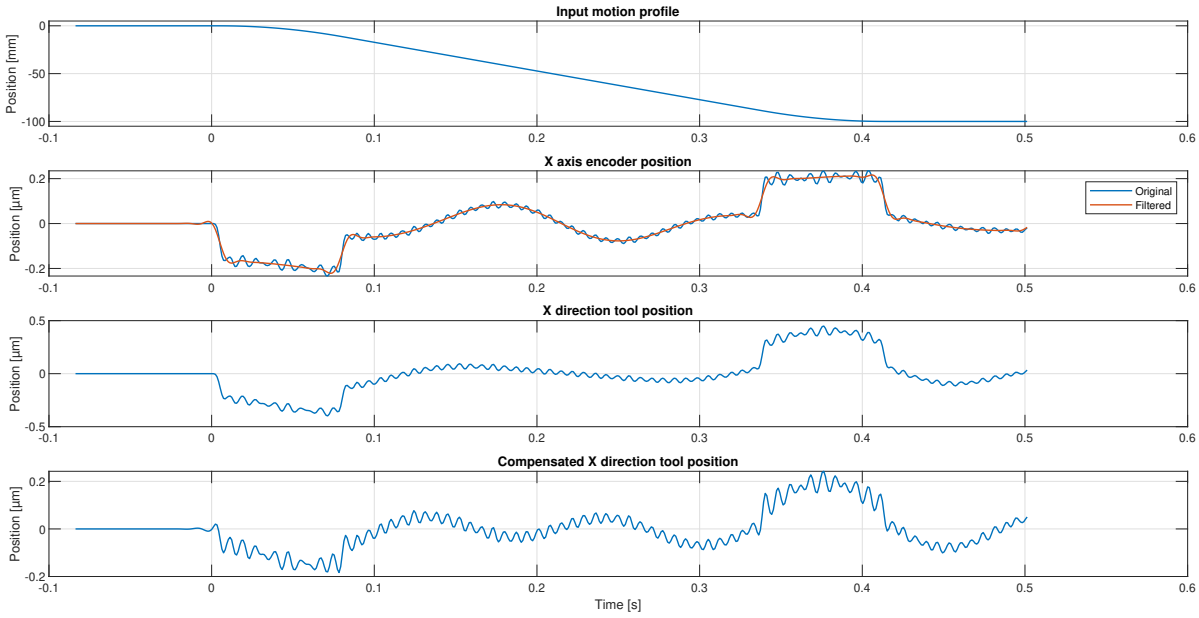

Figure 4.18: X direction simulation results

transform at low frequency. At 144 Hz a clear peak is seen in both figures. It is especially prominent in the bode plot of the constant velocity range. Another frequency that is visible in both figures is at 109 Hz. The difference between these two frequencies is 35 Hz, which matches with the beating pattern observed in figure 4.18. An interesting note is that the beating pattern is only visible within the acceleration peaks, but that both frequencies are well defined in the bode plots of both regions. Finally, 200 Hz is also quite visible in figure 4.20, and less so in figure 4.19. This frequency is not observed in the time domain.

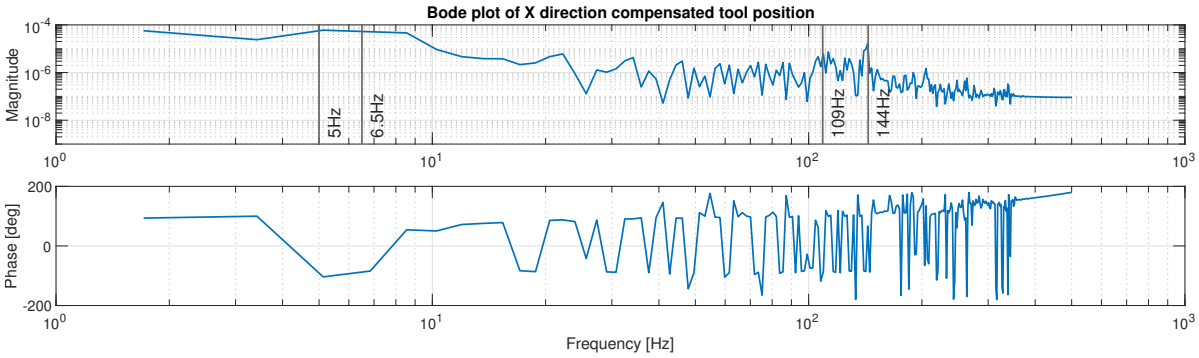

Figure 4.19: Bode plot of X direction compensated tool position, markers at 5, 6.5, 109 and 144 Hz

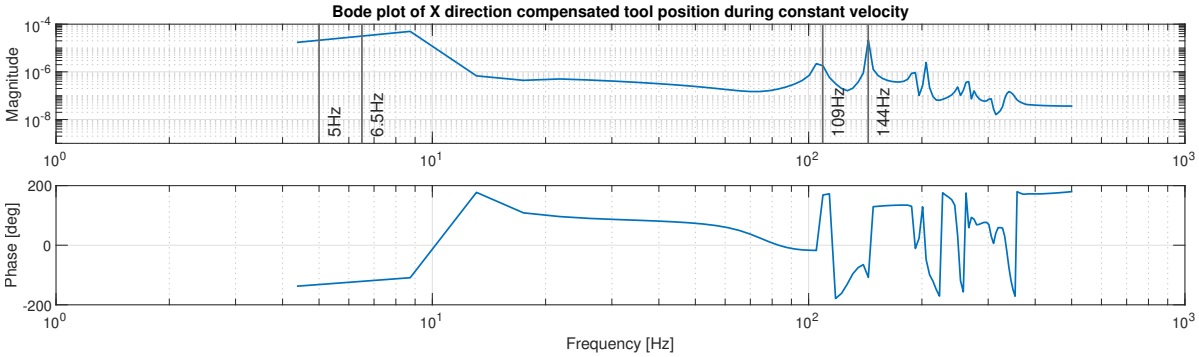

Figure 4.20: Bode plot of X direction compensated tool position during constant acceleration, markers at 5, 6.5, 109 and 144 Hz

4.1.6. X Comparison

Figure 4.21 shows the overlaid X direction tool positions found in the experiments and simulation. Compared to the Z direction, shown in figure 4.10, the signals differ more. Most notably, the displacement due to Z axis acceleration is in opposite directions. This will be discussed further in chapter 5. Secondly, the displacements due to acceleration differ roughly by a factor of 3. Finally, there is also a difference in vibration frequencies. An overview of these frequencies is given in table 4.2.

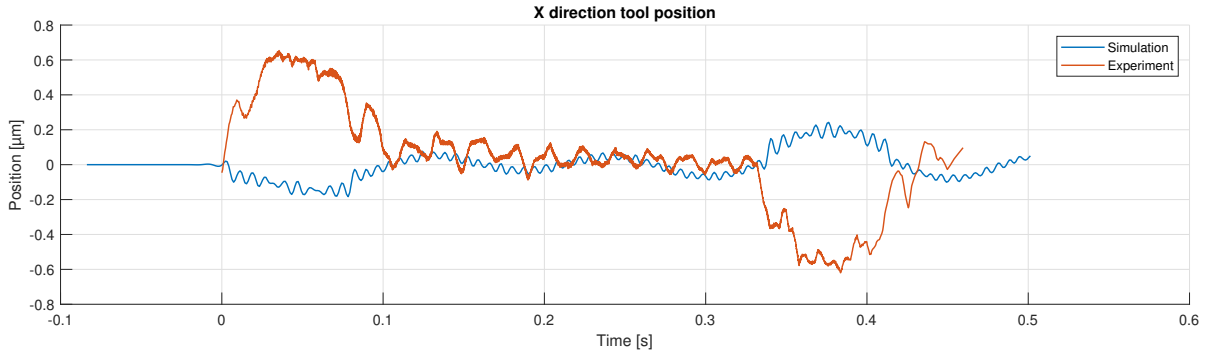

Figure 4.21: Comparison of X direction position

Table 4.2: Comparison of frequencies found in experiments and simulations [Hz]

	Experiment		Simulation	
X	47	160	5 - 6.5	109 - 144

Figures 4.22 and 4.23 show the overlaid experiment and simulation bode plots for a single stroke and constant velocity, respectively. Compared to the Z direction comparison, a larger difference in magnitude is visible. Analogous to the Z direction comparison, the figures indicate that the simulation model has lower damping than the physical machine. Again, the simulation bode plots are generally better defined as they contain no noise and have a higher sampling rate.

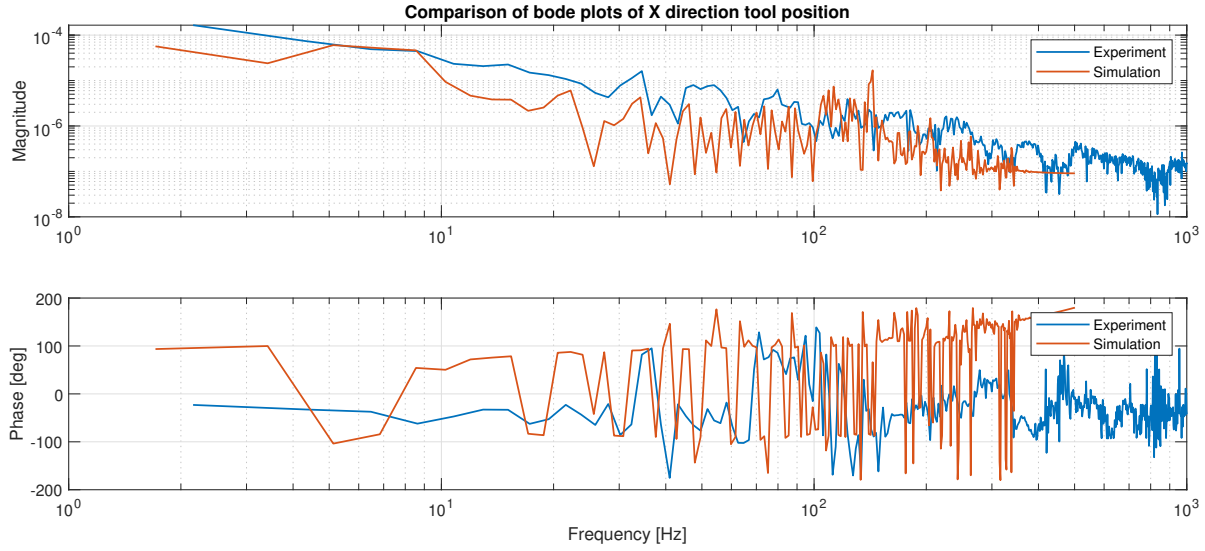

Figure 4.22: Bode plots of experiment and simulation results of X direction tool position

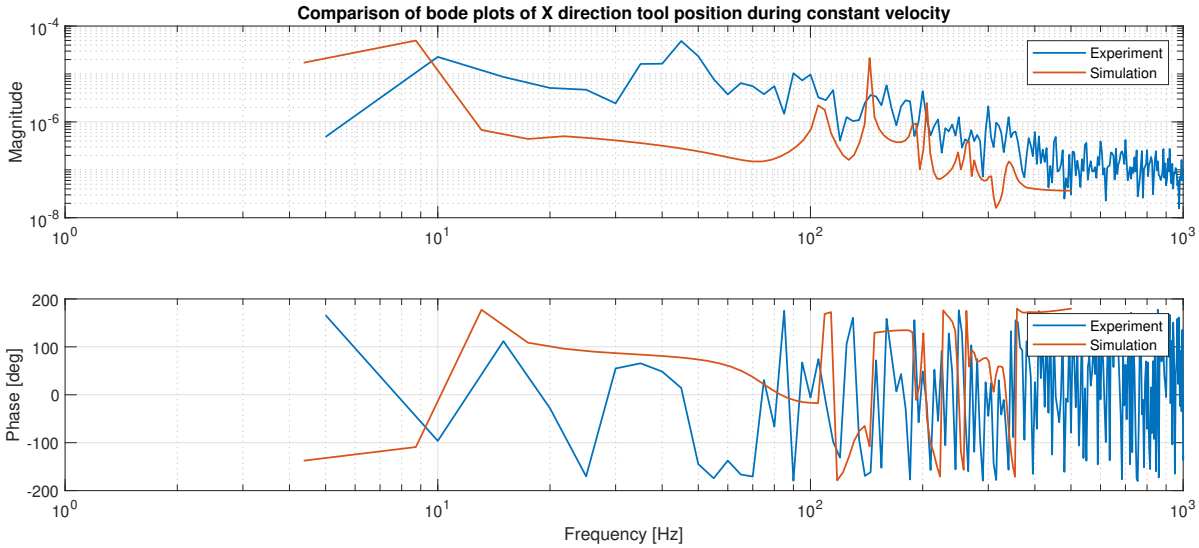

Figure 4.23: Bode plots of experiment and simulation results of X direction tool positon during constant velocity

4.2. Experimental results of multiple datasets

4.2.1. Z direction

In section 4.1 all analyses were done for dataset 10, since this was the dataset with the fastest motion profile, which is desirable for increased machine productivity. The same analyses can be applied to each of the nine dynamic datasets. Plotting the mean tool dynamic error for each dataset, figure 4.24 is created.

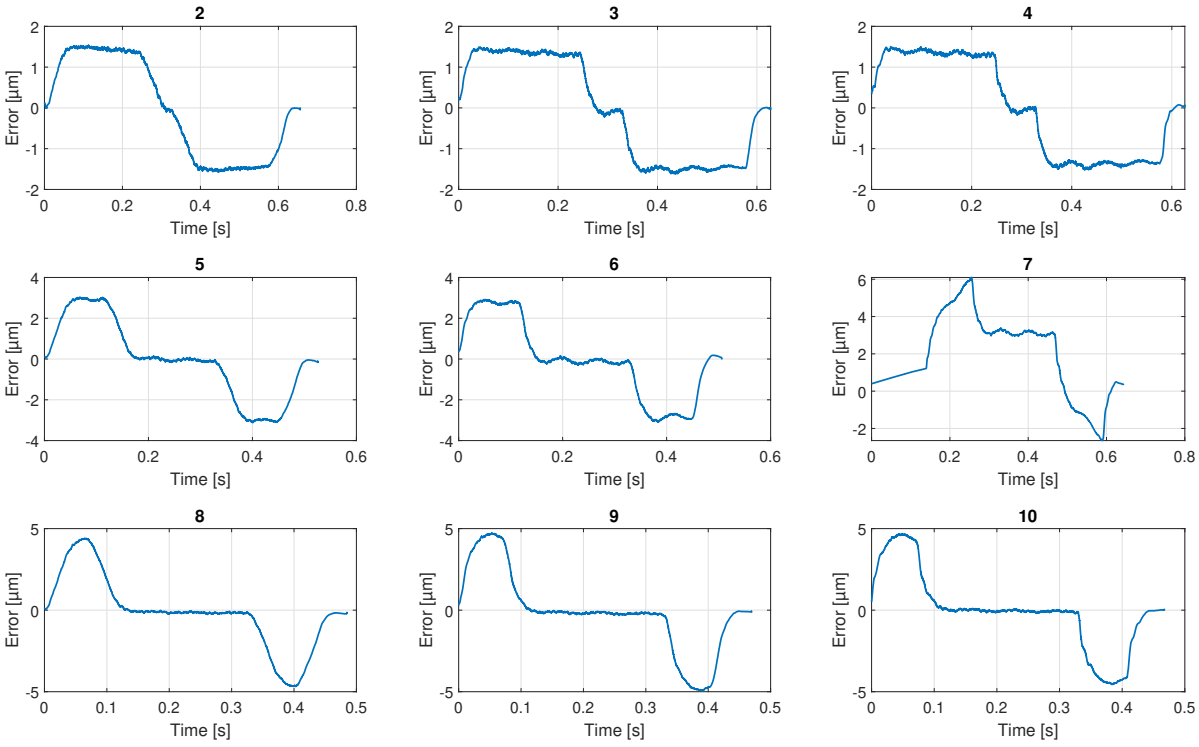

Figure 4.24: Mean tool dynamic error of all datasets

These mean tool dynamic errors can be used to gain insight in the influence of acceleration and jerk on the maximum amplitudes during acceleration and during constant velocity. As can already be seen in the figure, the maximum amplitudes differ only marginally in each row. Aside from this, the

mean tool dynamic error of dataset 7 very clearly differs from all other datasets. This is likely due to a programming error. Due to time constraints this error has not been sufficiently investigated. As such, this dataset will be excluded from the maximum amplitude analysis. However, the constant velocity section of these datasets does show behaviour similar to the other datasets. Since the mean value of the displacement during constant velocity is not investigated, it will be included in the analysis of maximum amplitude during constant velocity.

Although each dataset has a maximum value for jerk set in the controller, as described in table 3.2, there is no guarantee that this maximum is reached. To find the actual jerk value, the Z encoder velocity signal is differentiated twice with respect to time, for each stroke in each dataset. The average jerk value is then calculated for each dataset. An overview of the acceleration and jerk set in the controller and calculated jerk is given in the following table:

Table 4.3: Controller acceleration and jerk values and actual jerk value for each dataset

Dataset	2	3	4	5	6	7	8	9	10
Acceleration[m/s^2] - controller	1.2	1.2	1.2	2.5	2.5	2.5	4	4	4
Jerk [m/s^3] - controller	20	100	Brisk	55	275	Brisk	100	500	Brisk
Jerk [m/s^3] - actual	31	78	129	65	156	245	108	231	444

Figure 4.24 shows the mean tool dynamic error for each dataset. For each stroke in each dataset, the maximum and minimum values of the tool dynamic error are calculated. These values are then used to calculate an average peak height for each stroke. This yields a total of 10 values per dataset, of which the mean and standard deviation can be calculated. These mean maximum amplitudes and standard deviations, together with the corresponding jerk and acceleration values are used to create the overview in figure 4.25.

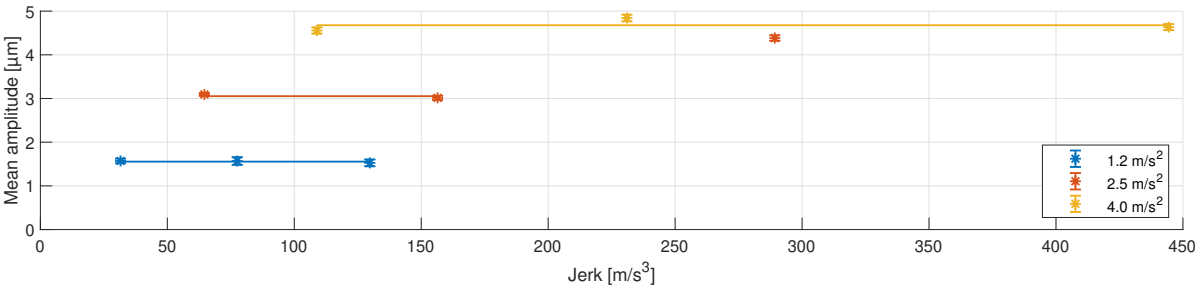

Figure 4.25: Mean amplitude and corresponding standard deviation for all datasets, 99.7% confidence interval

As can be expected, the maximum displacement of the tool during acceleration is mainly dependent on acceleration. The only outlier is the rightmost point of the 2.5 m/s^2 set. This is dataset 7 and as such this point will be ignored for this analysis. The figure also shows that this maximum displacement repeats very well, with a maximum 99.7% confidence interval of 0.2 µm. Lastly, the figure shows that the influence of jerk on the maximum displacement is negligible. As such, a horizontal line is drawn between datasets to emphasize these findings.

A similar approach can by applied to find the influence of jerk and acceleration on the displacement during constant velocity. Figure 4.26 shows the same Z direction tool dynamic error as figure 4.3b. For the range where velocity is constant the mean position and corresponding standard deviation can be calculated. Figure 4.26 contains horizontal markers for the mean value and confidence intervals of $\pm\sigma$ and $\pm 3\sigma$. This shows that the standard deviation can be used as a measure of vibration amplitude during the constant velocity range. Note that in this figure a slope is visible, which influences the standard deviation. This will be adressed in chapter 5.

The mean and standard deviation are calculated for each stroke in each dataset, which yields an array of 10 standard deviations for each dataset. The mean and standard deviation of this array can then be calculated. These values can be used to show the mean standard deviation of a dataset and to provide a corresponding confidence interval.

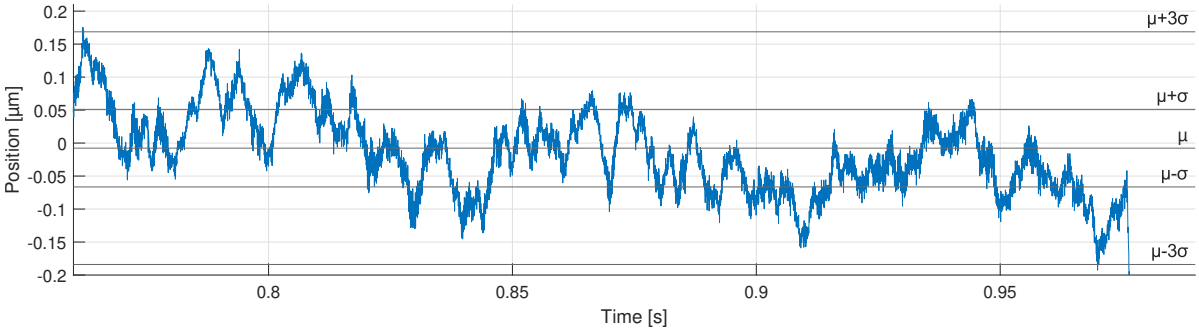

Figure 4.26: Single stroke tool dynamic error during constant velocity

This information can now be show the influence of jerk and acceleration on the mean standard deviation. This is shown in figure 4.27. As can be seen in figure 4.24, datasets 2-4 have very little constant velocity. The vibrations that are the subject of this analysis occur as a result of acceleration. This means that these accelerations also occur during constant (nonzero) acceleration. For datasets 2-4, both constant acceleration ranges are used for the analysis instead.

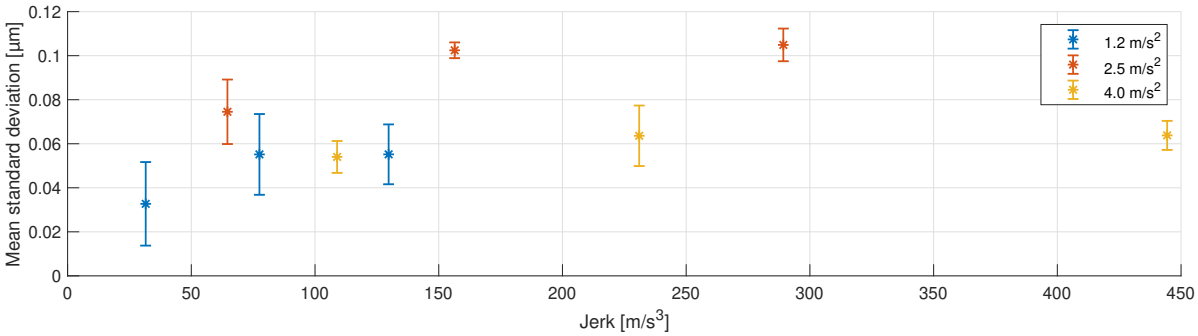

Figure 4.27: Mean standard deviations during constant velocity of all datasets, 99.7% confidence interval

In this figure a few things can be noted. Firstly, the mean standard deviation of the 2.5 m/s^2 datasets is higher than those of other acceleration settings. Although these results were automatically generated, this phenomenon is manually confirmed by looking at figure 4.24. Secondly, for each acceleration setting, a lower jerk value results in a lower mean standard deviation. Due to the size of the confidence interval, it would be possible to fit a horizontal line through the datapoints of the 1.2 and 4 m/s^2 sets. This will be discussed further in chapter 5.

4.2.2. X direction

The analysis of the X direction vibrations as a result of motion profile parameters is almost identical to the analysis for the Z direction. An overview of the mean X direction tool position is shown in figure 4.28. Note that for the X direction, dataset 7 looks as expected and will not be excluded.

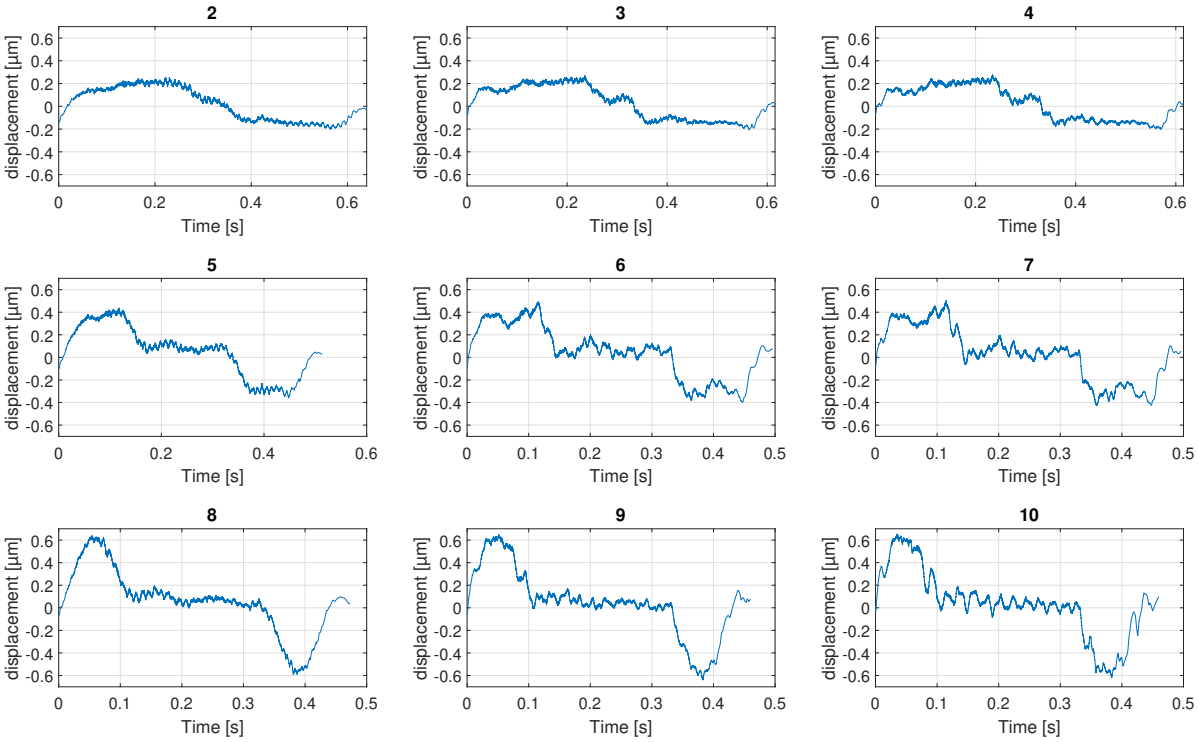

Figure 4.28: Mean tool position of all datasets

The actual jerk values for each dataset are calculated, as well as the mean amplitude due to acceleration of each dataset. Surprisingly, datasets 6, 7 and 10 had different jerk values compared to the Z direction experiments. This is shown in table 4.4.

Table 4.4: Controller acceleration and jerk values and actual jerk value for each dataset

Dataset	2	3	4	5	6	7	8	9	10
Acceleration[m/s^2] - controller	1.2	1.2	1.2	2.5	2.5	2.5	4	4	4
Jerk [m/s^3] - controller	20	100	Brisk	55	275	Brisk	100	500	Brisk
Jerk [m/s^3] - actual	30	76	132	64	186	272	108	231	416

With this information, figure 4.29 is created.

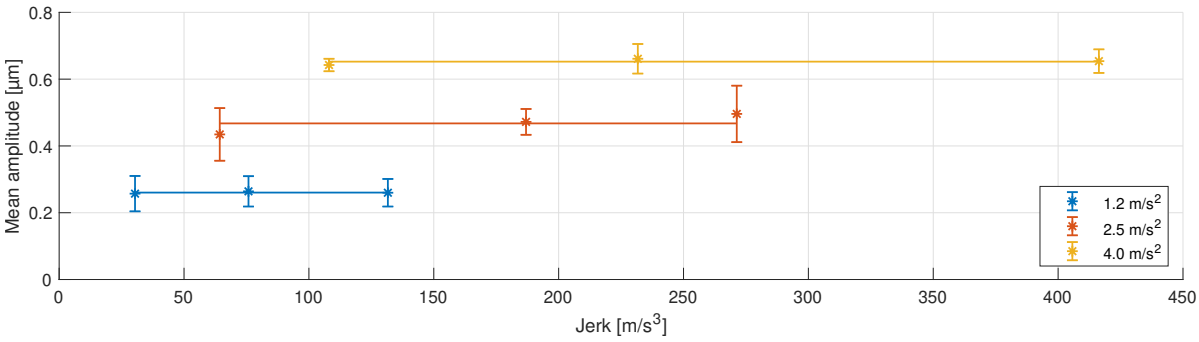

Figure 4.29: Mean amplitude and corresponding standard deviation for all datasets, 99.7% confidence interval

In this figure again a linear relation is seen between mean amplitude and acceleration. The influence of jerk on mean amplitude is again negligible.

The vibrations occurring during constant velocity can be analysed analogous to the Z direction analysis. In this analysis, the constant velocity range is used for all 9 datasets, as there is a visible curve in the constant acceleration range of the first three datasets.

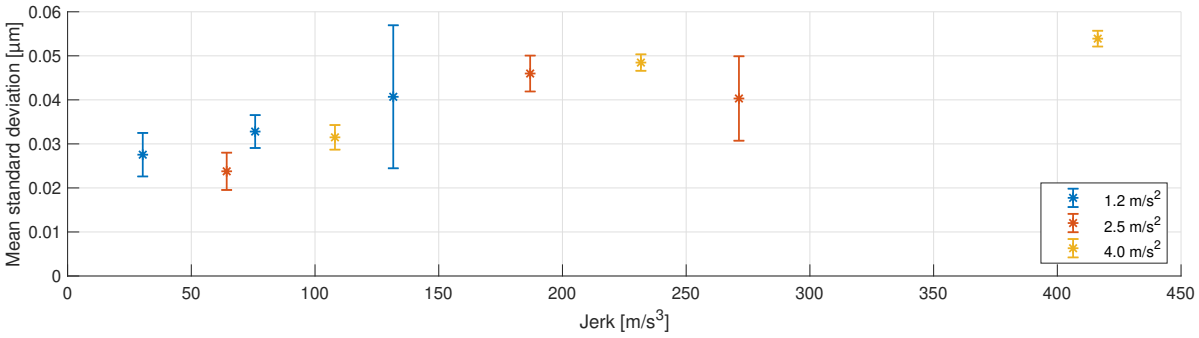

Figure 4.30: Mean standard deviations during constant velocity of all datasets, 99.7% confidence interval

In this figure a clear influence of jerk on the mean standard deviation is visible. Unlike the result of the Z axis analysis, the mean standard deviations of the 2.5 m/s^2 set lie between those of the 1.2 and 4 m/s^2 sets.

5 Discussion

In this chapter the results of the experiments and simulations will be discussed. This is followed by a discussion on the methodology, which is followed by a proposal for a new framework for experimental machine performance validation.

5.1. Fastest motion profile

Analogous to the results, this section is divided in two parts. The results of the fastest motion profile are discussed first, followed by a discussion on the comparison of all motion profiles.

5.1.1. Vibration frequencies and amplitudes

Table 5.1 contains the frequencies found in the fastest motion profile experiments and simulations.

Table 5.1: Comparison of frequencies found in experiments and simulations [Hz]

	Experiment			Simulation	
X		47	160	5 - 6.5	109 - 144
Z	14	47	100	6.5	106

Several things stand out from this table. First, there is a large difference in lower frequency between the Z experiment and simulation. Secondly, the simulation results have no equivalent for the 47 Hz vibration observed in the experiments. Finally, no vibration close to 14 Hz is observed in the X direction experiment.

Internal research projects have shown that the low frequency vibration visible at the Z encoder has a frequency close to the first eigenfrequency of the overall system. This is around 14 Hz for the experiment and between 5 and 6.5 Hz for the simulation. This indicates that the modelled stiffness of the rubber elements on which the granite base is mounted should be increased to better match the experiment.

In the experiment results of both the X and Z directions a 47 Hz vibration is visible. This vibration is not found by Vermeulen [13]. As can be seen in the results, the 47 Hz vibration is visible in the Z direction following errors of the encoder and tool, but not in the Z direction tool dynamic error. This means that the frequency has the same phase and amplitude at these two locations. It is also visible in the position signals of the X axis encoder and tool X direction, though with a smaller amplitude compared to the Z direction. With a lead of 6 mm and a velocity of 18 m/min, the rotational frequency of the Z axis ballscrew is 50 Hz. A minor misalignment or defect in the nut that travels over the Z axis ballscrew could force this 47 Hz vibration trough the system. This also explains why this frequency is not visible in the simulation results, as this defect or misalignment is not included in the model.

The X direction simulation indicates that a low frequency vibration should be visible at the X axis encoder and tool X direction. In the simulations, this frequency is observed at the tool in both X and Z directions. Therefore a frequency at or around 14 Hz should be visible in the X direction experiments as well. When comparing the Z direction experiment and simulation, the amplitude of this vibration is

significantly smaller in the experiment. It is likely that the X direction amplitude would therefore also be significantly smaller than amplitude found in the simulation. The most likely explanation for the absence of a visible 14 Hz vibration in the X direction experiment is that this vibration is present in the signal, but is overshadowed by the 47 Hz vibration.

The higher frequency vibrations found in the experiments and simulations match well. For the Z direction, they differ 6%. For X, this is 10%. The difference between these values can be attributed to modelling inaccuracies in the simulation, which will be addressed in section 5.3. Similar vibration frequencies were found by Vermeulen [13] for a different but similar machine. In his experiment he found the eigenfrequency of the Z axis ballscrew to be between 109 and 131 Hz and that of the X axis ballscrew to be at 200 Hz. He also indicated that these frequencies are dominant in their respective directions, but can also be observed in other directions. This is visible in the X direction experiment, where a 109 Hz vibration is seen alongside the 144 Hz vibration.

Finally, figures 4.10 and 4.21, which show the overlaid experiment and simulation results for the Z and X directions respectively, show that the amplitudes of all free vibrations are larger in the simulation. Together with mismatches in frequency this indicates that the stiffness and damping of internal machine elements are not yet modelled correct. This will be discussed in section 5.3.

5.1.2. Excitation direction of the tool in X direction

Figure 4.21 shows the overlaid X direction tool positions of the experiment and simulation. This shows that the direction in which the tool moves during acceleration in the simulation is opposite to what occurs during in the experiment. A probable cause for this is the location of the center of gravity of the X axis assembly with respect to the Z axis ballscrew. Not all components mounted on the X axis carriage were included in the finite element analysis. These elements were excluded because their individual mass were estimated to not influence the simulation results significantly. Figure 5.1 shows how the location of the center of gravity changes when several components that were excluded from the simulation are included in the X axis assembly.

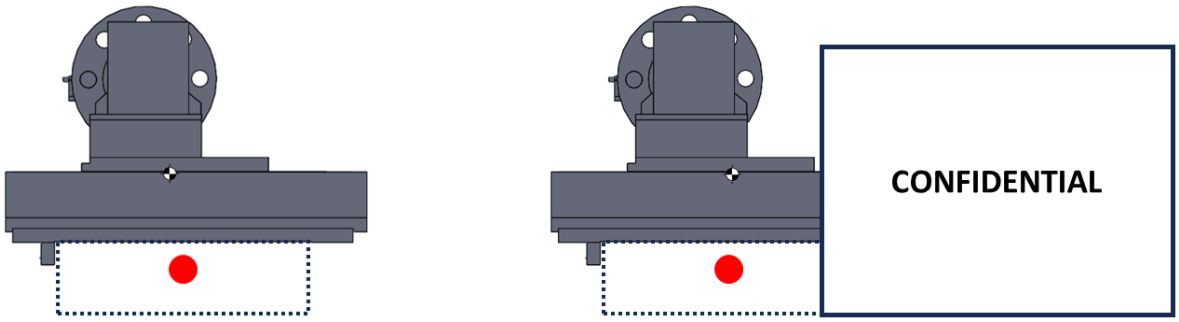

Figure 5.1: Influence of additional components on the center of gravity of the X axis assembly. Z axis slide indicated by blue outline, Z axis ballscrew indicated by red circle. The center of gravity shifts to the right of the Z axis ballscrew when additional components are added.

This phenomenon could also explain the difference in magnitude of the X direction tool positions during acceleration. The greater the distance in X direction between the X carriage assembly center of gravity and Z axis ballscrew, the greater the displacement. Including the sheetmetal plating of the X axis in the analysis would shift the center of gravity further to the right. Due to time constraints the finite element model has not been updated to investigate this hypothesis.

5.1.3. Influence of controller settings

Aside from the results found in these experiments and simulations, the difference in amplitude with the initial test in figure 3.1 should be noted. In this initial experiment, the following error between the encoder and controller setpoint has been measured to determine the influence of tool-material contact. This showed a clear vibration with an amplitude of around 3 µm. The later experiment shows that the tool following error has an amplitude of 0.5 µm. These measurements were performed on similar machines with different internal controller settings. The main difference between the geometries of these machines is an increase in the Z direction rubber element stiffness. Compared to the original machine, this should increase the frequency that corresponds to the rigid body mode and decrease

the amplitude of this vibration, but not by a factor of 6. This leaves the settings of the numerical controller. Further research on the influence of these controller settings should be conducted, which will be recommended in chapter 6.

5.2. Comparison of all motion profiles

Now that the results of the fastest motion profile have been discussed, the results of all datasets should be discussed. In chapter 4, the impact of jerk and acceleration on tool dynamic error and tool position has been investigated for two separate ranges in time. First, during a full stroke of the Z axis, focusing on the displacement as a result of acceleration. After this, the range in time is decreased to the section where velocity is constant. These results will be discussed in the same order. For conciseness sake, tool dynamic error and tool position will both be referred to as tool displacement in this section.

5.2.1. Displacement due to acceleration

The influence of acceleration and jerk on the tool displacement that occurs during acceleration is shown in figures 4.25 and 4.29, respectively. Aside from dataset 7 of the Z direction analysis, which was excluded from the analysis, all results in these figures indicate that jerk has negligible influence on the tool displacement during acceleration. During these parts of the motion profile, they are a forced vibration. This makes sense, as force equals mass times acceleration.

From these figures, another conclusion can be drawn. The figures show acceleration and the change in tool position. This change in position occurs as a result of a force, acting on a structure which has a certain combined stiffness. This gives two expressions for force, that can be combined:

$$F = ma = kx$$

Here m is the mass of the excited structure, a is the acceleration, k is the structures combined stiffness and x is the tool displacement that occurs during acceleration. This can be rewritten to show that the quotient of acceleration and corresponding change in tool position is a constant, namely the squared natural frequency of the corresponding eigenmode:

$$\frac{a}{x} = \frac{k}{m} = \omega_n^2$$

For all valid Z direction datapoints in figure 4.25, this results in a mean undamped natural frequency of 144 Hz, with a standard deviation of 3.7 Hz. For all X direction datapoints in figure 4.29, this is 370 Hz, with a standard deviation of 23.5 Hz. The larger standard deviation is likely due to the relatively small displacement, combined with the additional visible vibration on top of the displacement due to acceleration, which influences the measured maximum displacement. This matches with results found by Vermeulen [13]. For a different but similar machine, he found the structural resonance frequency of the Z axis to be between 121 and 145 Hz. A combination of an eigenmode and rigid body vibration at 375 Hz was also noted, which he predicted would be visible at the encoder and at the tool. Figures 4.22 and 4.23 contain peaks around this frequency, indicating that this prediction was correct.

5.2.2. Displacement during constant velocity

Although displacement during acceleration is interesting, cutting generally happens during constant velocity. This means that the vibrations that occur in that range are most influential on the cutting process. Figure 4.27 shows the mean standard deviation of Z direction tool dynamic error as a function of jerk and acceleration. This figure shows that for all three acceleration settings, there is an increase in standard deviation between the first and second jerk setting, whereas no such increase is observed between the second and third jerk setting. For 1.2 and 4 m/s^2 the confidence intervals of the datapoints allow for a horizontal line to be fit through them. For 2.5 m/s^2 this is not the case. Addition experiments are required to get a better understanding of the relationship between these variables. Another noteworthy result is that the mean standard deviation of the 2.5 m/s^2 set is significantly higher than that of the other two sets. As described in section 4.2.1, these results were manually confirmed. Further investigation of this phenomenon is left as future work.

In figure 4.26, which shows the worst-case dataset Z direction tool dynamic error during constant velocity, a drift in tool dynamic error is visible. This drift is present in all datasets of both measurement directions, in figures 4.24 and 4.28. This is most likely caused by thermal effects between when the

quasistatic and dynamic datasets were performed. As a result, the standard deviations of the tool dynamic error (Z) and tool position (X) for each stroke are larger than what they would be if no drift was present. The smaller the vibration amplitude, the more influence this drift has on the analyses of tool dynamic error during constant velocity.

The same analysis can be done for the X direction. Figure 4.30 shows a more random pattern when compared to the Z direction. This is likely due to the fact that the amplitudes of these vibrations are relatively small, which increases the influence of drift in the signal when compared to the Z direction. For this direction the mean standard deviation increases with acceleration.

Another source of error that influences these results is the length of time where velocity is constant. For all datasets with 1.2 m/s^2 acceleration, there is very little constant velocity in each stroke. Low frequency vibrations are therefore not visible in this region, even though they could have an impact on the standard deviation.

5.3. Methodology

In the previous sections the results of the experiments and simulations have been discussed. These results were created using a set of measurement and simulation methods that have been specifically designed for this purpose. In the following section, this methodology will be discussed.

5.3.1. Experiments

The experiments consist of measurements with additional sensors and components that were previously only used for (quasi)static measurements in the company. These measurements often need additional postprocessing to be able to extract useful information. A slight difference in compensation can heavily influence the results. These points, along with other general points of improvement, will be discussed below.

Compensating datasets

Various methods of data manipulation are applied to several signals to extract useful information from them. In chronological order, these are: Matching the clock speed of the NC and external data acquisition system, interpolating the signals of the external measurement system to match the (lower) sampling rate of the NC, compensating the dynamic readings with a compensation table created from multiple quasistatic measurements and finally compensating for the delay between two measurement systems and calculating the tool dynamic error. Each of these steps is a potential source of error and as such it is of utmost important that each step is considered and analysed carefully.

First, the quasistatic measurement was executed. In this measurement the sensor moved over the same range as the dynamic motion profiles, but with low velocity. The accelerations and decelerations at the the end of each stroke still produce forces and thus influence the dataset that is supposed to compensate all systematic error. Additionally, the NC is set up in such a way that it tries to maintain in movement while staying within a certain tolerance of the specified path. This tolerance allows the NC to deviate, which in turn influences the quasistatic dataset. These two issues can be circumvented by extending the movement range of the quasistatic dataset and adding pause commands between each of the movements, forcing the NC to completely halt all movement.

Furthermore, creating one compensation table to compensate for systematic error has proved to not be sufficient. Conducting all experiments in a single direction took multiple hours. In this time, a slight variation in temperature has introduced additional systematic error. This in turn influences the results. It is possible to fit a line through the drift that this creates in each stroke and use this line to compensate for the additional systematic error. Nevertheless, it is better to prevent this issue entirely. An improved method of compensating for systematic error is proposed in section 5.4.

Finally, a drawback of calculating the Z direction tool dynamic error is that this does not only compensate for any delay in the NC, but also removes all mechanical delay caused by inertia in the system.

Measurement range

The most important section of the tool dynamic error and tool position is during constant velocity. All motion profiles used in this thesis had a travel distance of 100 mm. As a result, motion profiles with low acceleration contained very little constant velocity. When this range in time is shorter than one period of the lowest vibration present, these vibrations cannot be observed during the analysis, causing a

lower mean standard deviation in the analysis. Where possible, the range in position where velocity is constant should be kept identical over all motion profiles.

Bending of the ground shaft
The ground shaft that is sensed by the capacitive sensor in the X direction measurement is a cantilever. Even though the forces that result from acceleration are mainly in the axial direction of this shaft, the capacitive sensor readings are likely influenced by the elastic deformation of the shaft. This deformation is expected to be negligible, but should be included in future research to confirm this suspicion.

Finding frequency information
To find which frequencies are present in a signal, two methods have been used. First, peaks in these signals have been counted manually over a certain period in time. Secondly, the signals have been analysed in the frequency domain using the Fourier transform. An inherent problem with analysing these type of signals in the frequency domain is highlighted by the many bode plots in chapter 4. The tool dynamic error and tool position contain sharp corners in displacement due to acceleration, which resemble those of a square wave and contain a large range of frequency content [24, 25, 26]. Even though the corners of this signal are not as sharp as those of a square wave, a high frequency content is still contained within them. Additionally, the range in time that contains the vibrations that are visible in the time domain is short compared to the complete signal. A Fourier transform of the complete signal contains a myriad of frequencies that occur elsewhere in the time signal. This makes it hard, if not impossible, to distinguish the relevant frequencies. Isolating the relevant range in time from the complete signal - either the tool dynamic error or tool position of a single stroke, or the constant velocity portion of that stroke - reduces the total number of points in the frequency domain. As a result frequencies are less defined in the bode plot, especially at the lower end of the spectrum. At the same time, the influence of unrelated frequencies is smaller, resulting in more prominence of the relevant frequencies when their frequency is sufficiently high.

For this thesis, the only signal conditioning that was applied before the Fourier transform was a subtraction of the signal mean. Additional avenues that could be explored to improve the Fourier transform results are zero padding [27] and window functions [25].

Following error and tool dynamic error
As described in section 2.6, the following error is the difference between the position setpoint and actual position and the tool dynamic error is the difference between the encoder and tool position. For the Z direction, this thesis has mainly focused on tool dynamic error. For the X direction, the focus was on tool position, as no motion profile was visible in this signal. It is important to note that the Z direction tool dynamic error does not indicate the total displacement of the tool, but rather the difference between the encoder and the tool positions. This is illustrated by the fact that the 47 Hz vibration is not observed in the experiment tool dynamic error, but is observed in the following error of the encoder and tool, as seen in figures 4.3 and 4.2, respectively. This indicates that the effect that causes this vibration has equal influence on the Z direction encoder and tool positions.

Both the tool dynamic error and following error are interesting for machine performance validation. The tool dynamic error gives a measure for the increase of vibrations at the tool, as well as any additional vibrations occurring at the tool. On the other hand, the tool following error provides insight on the complete difference in tool position. Comparing the following error in figure 4.2 to the tool dynamic error in figure 4.3, one observes that the following error is constant for a shorter range in time compared to the tool dynamic error.

Additionally, the following error has a shape that resembles the velocity profile, similar to the difference between encoder and tool positions. While the difference between the encoder and tool positions is the result of delay between two measurement systems, the shape of the following error is a result of the control system [28]. It may be possible to compensate for this trapezoidal shape and use this as a measure for total tool displacement during the full motion profile. This is left for future research.

5.3.2. Simulation model

The finite element model is designed to emulate the experiments. As described in the third chapter, this not only includes the model geometry and using a third order motion profile as an excitation source, but also an emulation of the tool sensors in their respective directions. For the laser interferometer, this is done by evaluating nodes on the beamsplitter and retroreflector. For the capacitive sensor, this is done by having the model of the sensor touch the target, specifying a negligible stiffness for this contact and evaluating the interface over time. In the following paragraphs any issues with the model and these methods will be discussed, so that they may be addressed in future research.

Model inaccuracies

The comparison of experiment and simulation results in section 5.1 indicate a difference in mass, stiffness and damping. As seen in that section, this is mostly related to the properties of the set of rubber elements. Getzner [29] indicates that the stiffness of rubber elements is dependent on the preload, as well as the loading frequency. This could explain the large difference between the simulation and experiment frequencies and should be investigated further to increase model accuracy. Additionally, each machine component is currently defined to have global contact. In reality, the interface between components provides additional damping to the system. Adding appropriate contact conditions between all components would likely increase model accuracy. However, this is quite labour intensive and mainly influences the amplitude of vibrations.

Another model inaccuracy that was highlighted by the simulation results is the missing components of the X axis assembly. The absence of these components has shifted the center of gravity of the X axis assembly to the other side of the Z axis ballscrew, resulting in simulated motion in the opposite direction.

A final inaccuracy of the current model is the way the X axis ballscrew stiffness is implemented. As discussed in section 3.4.3, the Z axis ballscrew is emulated using a virtual stiffness, acting between the two faces that this ballscrew would be mounted between. For the X axis ballscrew, this is not the case. The bearing pads of the X axis carriage have been defined as having a stiffness in the X axis direction. The method that has been implemented for the Z axis could also be implemented for the X axis, with a desired displacement of 0 m during the entire study.

A body-fixed coordinate system

As described in section 3.4.3, several nodes are evaluated at each point in time and subsequently imported in MATLAB to create a local coordinate system that maintains alignment with the X and Z axes of the machine, so that other nodes can then be evaluated in this local coordinate system. The issues with this approach are described below.

The nodes that are used to define the local coordinate system are orthogonal at the start of the simulation. As soon as forces are introduced, this may no longer be the case. Figure 5.2 shows the variation of the angle between the X and Z axes. As most nodes of interest are around 1 m from the origin, the figure also shows the error of a point at that position. The maximum error of around 0.05 µm is deemed negligible for this thesis.

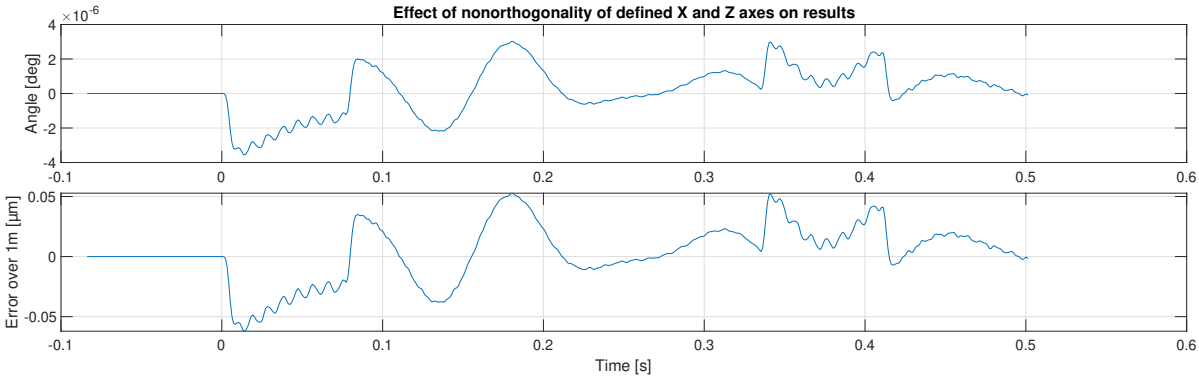

Figure 5.2: Influence of non-orthogonality of X and Z axes on point 1 meter from origin

Another issue is that the driving force and evaluation of capacitive sensor displacement are in their respective global directions. This means that as the machine rotates during the simulation, a mismatch in directions is created. This rotation is likely quite small, but as the influence of small angular errors increase over distance, this issue should be investigated in future research.

Tool dynamic error and compensated tool position

In the Z direction simulation the difference between filtered encoder following error and tool following error is calculated to approximate the tool dynamic error. In the X direction, the actual tool position is approximated by subtracting the filtered encoder position from the tool position. These filtered signals are the signals that a controller could compensated. Subtracting these filtered encoder signals from the tool signals has several caveats.

When the controller detects a following error, it will generate an additional torque on the motor at the next timestep to compensate for this error. This torque influences the machine and thus the position of the tool, which is not controlled by the controller. Compensating after the fact results in a different signal than when the controller can compensate at each timestep.

Additionally, there is a frequency-dependent amplification effect between the encoder and tool. Vermeulen [13] has researched this for a similar machine and found that for frequencies between 30 and 100Hz, the amplification factor increases from 0.98 to 1.05 in the X direction and from 1 to 1.2 for the Z direction.

Finally, depending on the control system, each frequency is compensated a different amount. A frequency close to the controller bandwidth will have more influence on the overall system than a frequency of equal amplitude far below the controller bandwidth.

Goal of the simulation model

Although the previous sections mention plenty of points of improvement for the simulation model, it is important to not lose focus of the goal of the model. As presented, the vibration frequencies and corresponding amplitudes do not match with those found in the experiments. However, the model does already exhibit the same behaviour as the experiments and the differences can be explained with the current knowledge. With this, the model can already be used to evaluate the relative effect of changes to the machine structure. When deciding which of the aforementioned improvements should be implemented the effect on the overall goal, as well as the required effort for implementation, should be considered.

5.4. Framework for experimental machine performance validation

A substantial part of this thesis is dedicated to creating new testing methods to analyse machine dynamics. The results of these analyses can be used as a new baseline for machine performance validation. There are many intricacies to setting up these experiments and analysing the produced data. With the lessons learned from the experiments in this thesis, the following experiment method is proposed as framework for future research and performance validation.

Setting up the X and Z direction experiments and data acquisition

1. Mount and align the additional sensor, which measures tool position, in the machine. Confirm that the signal strength is sufficient over the full measurement range.
2. Set up data acquisition from the controller and from the additional sensor.
3. In the NC data acquisition system, make sure to keep signals that will be compared to each other next to each other in the list. Signals are not saved instantly, the delay between saving two signals may cause issues. This is minimized by choosing an appropriate acquisition order. This step can be skipped if future work confirms that the delay between signals acquired by the NC is sufficiently small.

Setting up the code that drives the machine

1. Apply the relevant parameter changes to the NC to ensure the correct motion profile is run by the controller.
2. At the start and end of all movement, quasistatically move the measured axis back and forth 10 micrometers. This movement is used to synchronise the two measurement systems, as well as compensate for any mismatch in clock speed of the measurement systems.
3. Apply a quastistatic movement over a longer range than the dynamic measurement range at the beginning and end of the dynamic movements. Increasing the quasistatic range prevents any influence of acceleration effects on the position measurement.
4. Repeat each dynamic motion profile multiple times. In this thesis, each motion profile is repeated 10 times.
5. Force a one second pause between each of the movements. Without this, the controller attempts to reach each programmed point while maintaining velocity within a certain range. To do this, the controller will deviate from the desired motion profile.
6. Make sure that the motion profile contains a sufficiently long portion of constant velocity, so that the vibrations that occur in this range can be properly isolated and analysed.
7. Keep the range of constant velocity identical for all motion profiles, meaning that a motion profile with lower acceleration moves a larger distance. This keeps all errors related to machine geometry such as straightness and perpendicularity of the axes, as well as other mechanical error sources constant over all datasets.

Figure 5.3 shows an overview of the proposed movements for the measurement of a single motion profile. Note that this figure is not to scale.

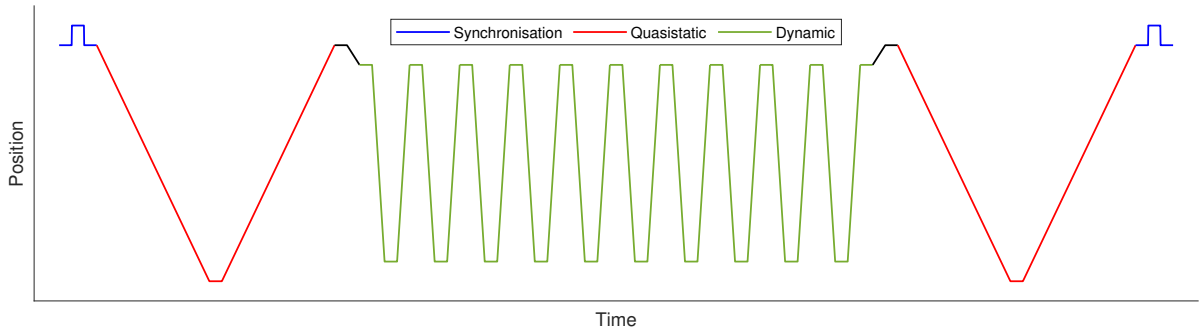

Figure 5.3: Overview of proposed Z direction movements, not to scale

Setting up the code that processes the data

1. Align datasets from both measurement systems using the first synchronisation peak.
2. Scale the time array of one of the measurement systems such that the second synchronisation peaks are aligned.
3. Identify and separate each consecutive motion profile (position data of both measurement systems, as well as any additional signals that are required for subsequent analysis) from both measurement systems.
4. Isolate the quasistatic motion profiles and use these to calculate the systematic error for each tool position of the motion profile. Then compensate each motion profile for this systematic error. These two quasistatic motion profiles can also be used to investigate the thermal growth that occurred during the experiment. If this growth is significant, consider creating a function that increasingly applies the difference of this thermal growth to each motion profile.

5. Calculate the actual peak jerk and acceleration values for each motion profile by differentiating the encoder velocity signal.
6. For the Z direction, calculate the tool dynamic error for each motion profile by comparing the position data of the encoder and tool. The delay between these signals should be accounted for using the method described in section 4.1.1. For the X direction, calculate the tool position.
7. Find the peak values of the tool dynamic error and tool position, caused by acceleration. Also calculate the mean and standard deviation of the position during constant velocity. Then find the mean and standard deviation of these values. Use this information, in combination with the peak jerk and acceleration values mentioned earlier, for the analysis as described in this thesis.

With this, the basic framework is set up. This can be expanded upon by analysing additional signals are included in the original datasets. Examples of these are following error, position setpoints and motor torque. Additionally, these signals can be analysed in the frequency domain.

6

Conclusion and outlook

6.1. Conclusion

In this thesis the origins and influence of vibrations present in a two-axis CNC lathe have been investigated. The scope was limited to vibrations at the tool and axis encoders, originating from machine movement, for which several experiment setups were designed and implemented. Additionally, a finite element model was created that approximates the machine geometry, measurement setup and excitation method. Although many improvements can be made to this model, it is already usable for investigating relative influence of machine redesign on tool vibrations.

The experiments identified vibrations of 14, 47, 100 and 160 Hz at the tool and X and Z encoders, with 14 and 47 Hz having the greatest amplitudes. While the 14 Hz vibration is related to the rigid body mode of the machine, the 47 Hz is hypothesized to originate from misalignment of the Z axis drive system. These vibrations were found to be dominant in Z direction, where a maximum displacement of the tool relative to the axis encoder of approximately 0.3 µm was found during the section of the motion profile where velocity - and thus cutting speed - was constant. In the X direction this maximum amplitude was calculated to be approximately 0.16 µm, although the true value is expected to be lower as the calculation is influenced by errors due to thermal growth.

Additionally, the influence of motion profile parameters on maximum tool displacement has been investigated during acceleration and during constant velocity of the Z axis. Once again, displacement in the Z direction was found to be dominant over the X direction. While displacement during acceleration was found to only be dependent on acceleration, jerk had a significant influence on displacement during constant velocity as the amplitude increased with increasing jerk.

Finally, the developed experiment setups and corresponding analysis tools were combined into a framework that aids in investigating the dynamic performance of two-axis lathes.

6.2. Outlook

With the introduction of the framework for evaluating dynamic performance of two-axis lathes, several clear avenues arise. Firstly, the framework and subsequent analysis can be expanded by investigating the influence of measurement order of signals in the NC on delay between these signals. Additionally, the influence of bending of the ground shaft in the X direction experiment should be investigated. To decrease measurement effort, automated writing of NC parameters and automatic triggering of measurements with the secondary measurement system can be investigated. Furthermore, the framework can be applied to investigate the effects of acceleration, jerk and other NC parameters on tool displacement for a larger range of parameter values and on multiple machines. Finally, specially tuned motion profiles can be created to maximize machine performance while keeping tool displacement below a set threshold.

Aside from expanding and applying the framework, the finite element model can be expanded to improve model accuracy so that it can be better used to investigate the influence of changes in the model and motion profile on tool displacement. First, the missing components of the X axis assembly can be incorporated. Furthermore, the rubber elements can be analysed further regarding their stiffness and damping properties under preload and cyclic loading. Experimental modal analysis can also be

used to indicate areas in which the model differs with reality. Contact stiffness and damping can be implemented to better match with this modal analysis. For this, implementation effort should be weighed against the expected increase in model accuracy. Finally, the finite element model can be validated against experiments for a range of motion profiles.

In addition to future work relating directly to the approaches applied in this thesis, there is also a vast amount of possible research regarding improving machine performance. These include, but are not limited to, expanding the control system with either feedforward control or more advanced feedback controllers and incorporating additional sensors close to the tool into the control system.

A

Rubber elements impulse responses

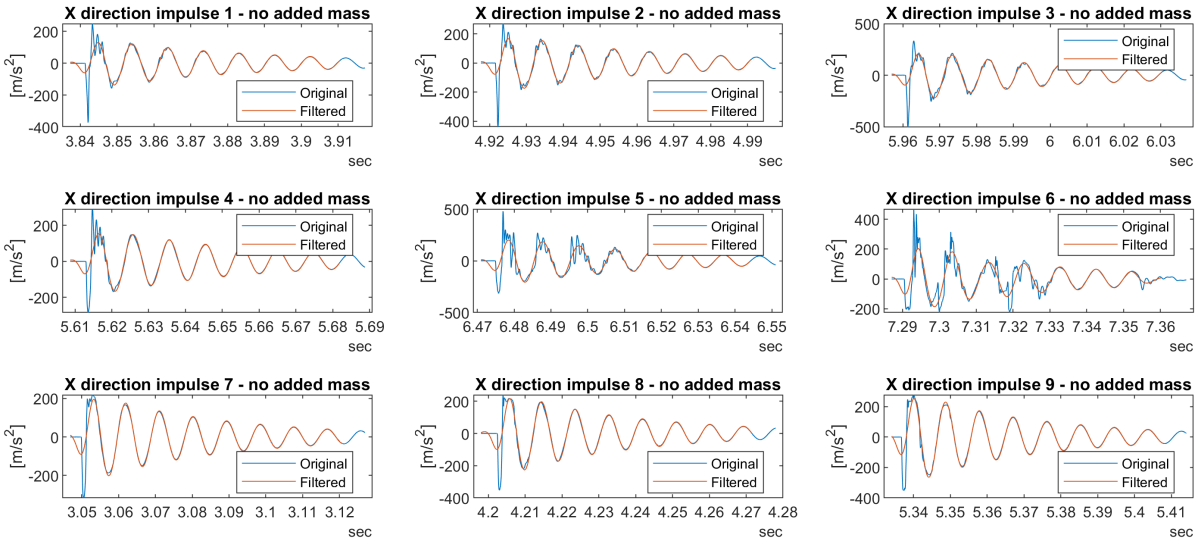

Figure A.1: X direction (lateral) impulses without added mass

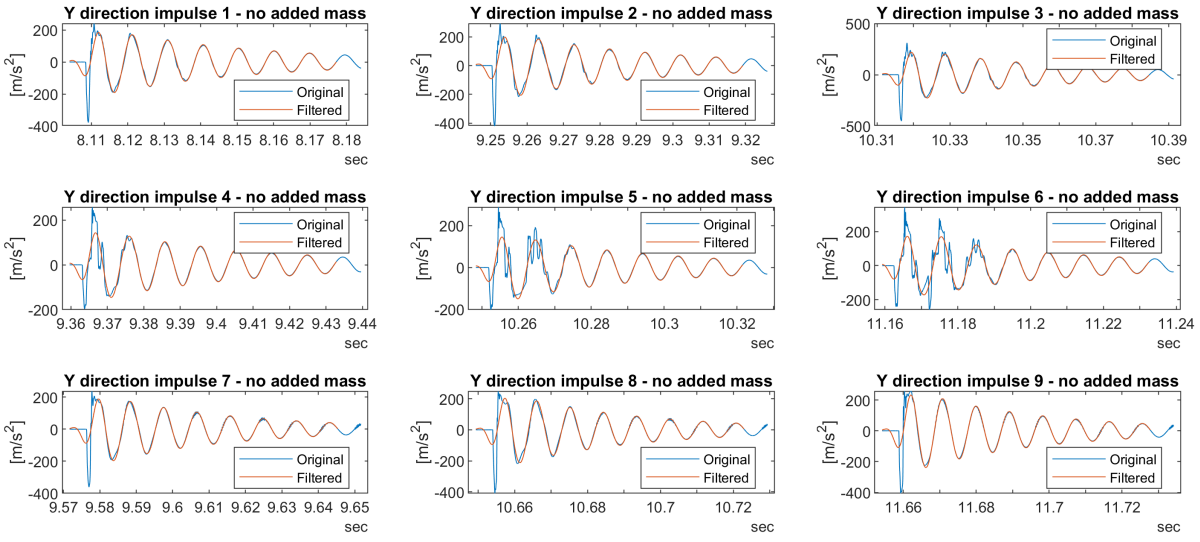

Figure A.2: Y direction (lateral) impulses without added mass

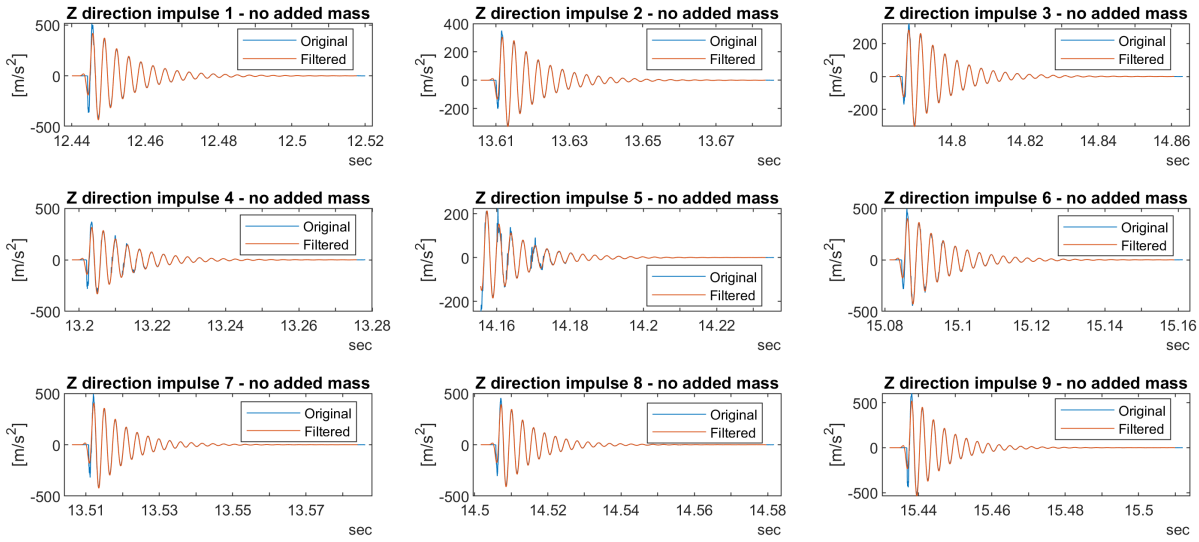

Figure A.3: Z direction (axial) impulses without added mass

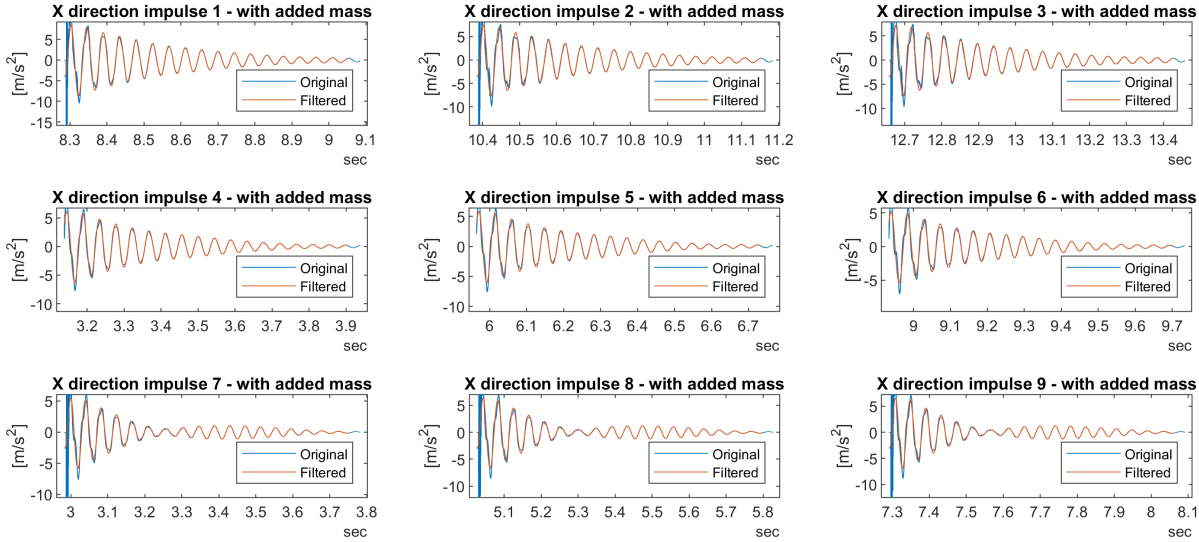

Figure A.4: X direction (lateral) impulses with added mass

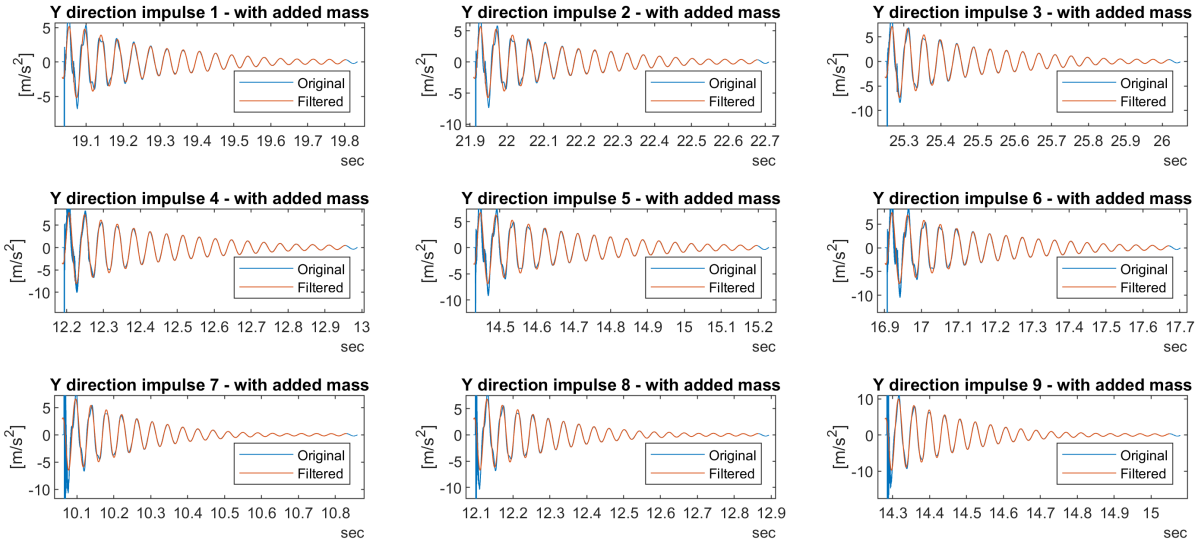

Figure A.5: Y direction (lateral) impulses with added mass

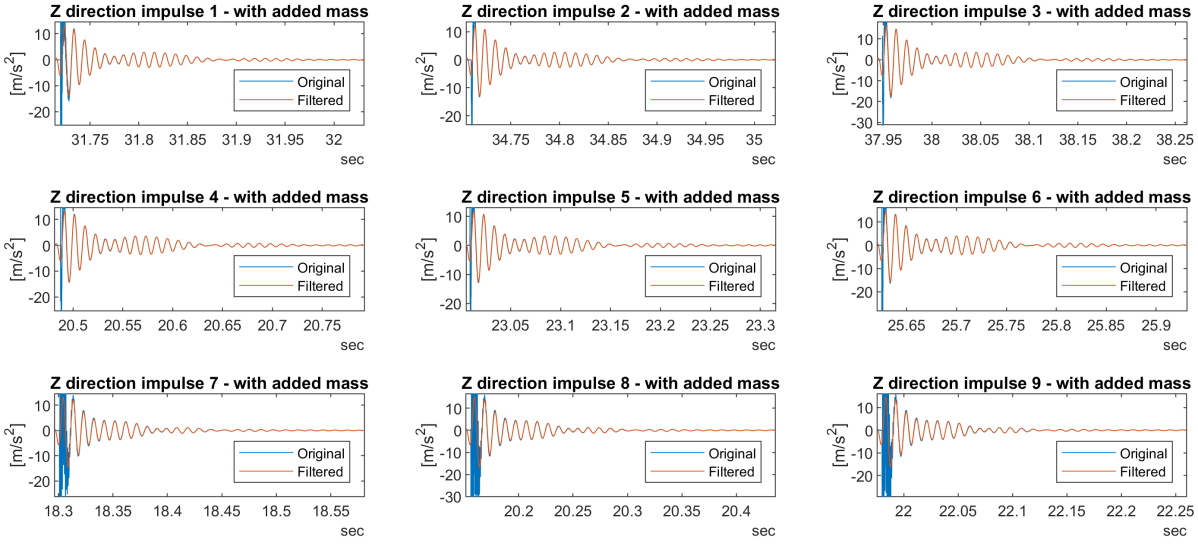

Figure A.6: Z direction (axial) impulses with added mass

Bibliography

[1] Brian Clifford. *A brief history of woodturning*. URL: http://www.turningtools.co.uk.wgo.ca/history2/history-turning2.html.

[2] Hembrug Machine Tools. *Hembrug Finish Hard Turning Machines - Corporate Brochure*. 2015.

[3] Yusuf Altintas. *Manufacturing automation : metal cutting mechanics, machine tool vibrations, and CNC design*. Cambridge University Press, 2012. ISBN: 9780521172479.

[4] COMSOL Multiphysics. *Structural Mechanics Module User's Guide*. 2021. URL: doc.comsol.com/6.0/doc/com.comsol.help.sme/StructuralMechanicsModuleUsersGuide.pdf.

[5] W. B. Rowe. *Hydrostatic, aerostatic, and hybrid bearing design*. 2012. ISBN: 9780123969941.

[6] Tungaloy. *General Catalog*. 2020.

[7] T Paul. *Cutter compensation for beginners*. Dec. 2018. URL: https://www.autodesk.com/products/fusion-360/blog/cutter-compensation/.

[8] International Organisation for Standardisation. *Test code for machine tools - Part 8: Vibrations*. ISO/TR 230-8:2010. Geneva, Switzerland, 2010.

[9] P A McKeown and G H Morgan. "Epoxy granite: a structural material for precision machines". In: *Precision Engineering* 1.4 (1979), pp. 227–229. ISSN: 0141-6359. DOI: https://doi.org/10.1016/0141-6359(79)90104-1.

[10] Sebastian Castro. *Trajectory Planning for Robot Manipulators*. Nov. 2019. URL: https://blogs.mathworks.com/student-lounge/2019/11/06/robot-manipulator-trajectory/.

[11] Siemens. *SINUMERIK 840D sl Servo Tuning with AST*. Mar. 2019.

[12] JPE. *Third order point-to-point motion profile*. URL: https://www.jpe-innovations.com/precision-point/third-order-point-to-point-motion-profile/.

[13] M P Vermeulen. *Dynamics of a machine tool cross-slide*. 2020. URL: http://resolver.tudelft.nl/uuid:9c2b5ebb-44b9-45c4-b6e8-64f069243d0b.

[14] Siemens. *SINUMERIK 840D sl / 828D Fundamentals Programming Manual*. Feb. 2011.

[15] Renishaw. *Interferometry explained*. URL: www.renishaw.com/en/interferometry-explained--7854.

[16] Wei Gao et al. "Machine tool calibration: Measurement, modeling, and compensation of machine tool errors". In: *International Journal of Machine Tools and Manufacture* 187 (2023), p. 104017. ISSN: 0890-6955. DOI: https://doi.org/10.1016/j.ijmachtools.2023.104017.

[17] L Nowakowski, M Skrzyniarz, and E Miko. "The analysis of relative oscillation during face milling". In: *Engineering Mechanics* 182 (2017), pp. 730–733.

[18] Jerzy Józwik, Ivan Kuric, and Andrzej Łukaszewicz. "Analysis of the Table Motion of a 3-Axis CNC Milling Machine Tool at Start-up and Braking". In: *Advanced Manufacturing Processes*. Ed. by Volodymyr Tonkonogyi et al. Cham: Springer International Publishing, 2020, pp. 108–117. ISBN: 978-3-030-40724-7.

[19] H F F Castro and M Burdekin. "Dynamic calibration of the positioning accuracy of machine tools and coordinate measuring machines using a laser interferometer". In: *International Journal of Machine Tools and Manufacture* 43.9 (2003), pp. 947–954. ISSN: 0890-6955. DOI: https://doi.org/10.1016/S0890-6955(03)00083-X.

[20] Renishaw. *XL-80 laser measurement system*. URL: https://www.renishaw.com/en/xl-80-laser-system--8268.

[21] Zongchao Geng, Zhen Tong, and Xiangqian Jiang. *Review of geometric error measurement and compensation techniques of ultra-precision machine tools*. 2021. DOI: 10.37188/lam.2021.014.

[22] Sebastian Böhl, Sascha Weikert, and Konrad Wegener. “Improving robustness of capacitive displacement measurements against electromagnetic disturbances in machine tool environments”. In: *Lamdamap* 13 (2019).

[23] Lion Precision. *Instruction Manual Modular System: Measurement Systems*. 1999. URL: https://www.lionprecision.com/manual-rd10-20-rd12-22-dmt10-20-dmt12-22/.

[24] Y Altintas et al. “Machine tool feed drives”. In: *CIRP Annals* 60.2 (2011), pp. 779–796. ISSN: 0007-8506. DOI: https://doi.org/10.1016/j.cirp.2011.05.010.

[25] National Instruments. *Understanding FFTs and Windowing*.

[26] Alan V Oppenheim, Alan S Willsky, and S Hamid Nawab. *Signals and Systems*. 2nd ed. New Jersey: Prentice Hall, 1996. ISBN: 0-13-814757-4.

[27] Wang Hongwei. *FFT Basics and Case Study using Multi-Instrument*. 2009.

[28] O Masory. “Improving Contouring Accuracy of NC/CNC Systems With Additional Velocity Feed Forward Loop”. In: *Journal of Engineering for Industry* 108.3 (Aug. 1986), pp. 227–230. ISSN: 0022-0817. DOI: 10.1115/1.3187068.

[29] Getzner. *Material Properties and Vibration Isolation - Technical Information*. Oct. 2018.